Geochimica et Cosmochimica Acta 374 (2024) 33–50

Contents lists available at ScienceDirect

Geochimica et Cosmochimica Acta

journal homepage: www.elsevier.com/locate/gca

Towards a new impact geochronometer: Deformation microstructures and U-Pb systematics of shocked xenotime

Cilva Joseph [a,b], Denis Fougerouse [a,b,*], Aaron J. Cavosie [a,c], Hugo K.H. Olierook [a,d], Steven M. Reddy [a,b], Tommaso Tacchetto [a,b], Raiza R. Quintero [e], Allen Kennedy [d], David W. Saxey [d], William D.A. Rickard [d]

[a] School of Earth and Planetary Sciences, Curtin University, Perth, Australia
[b] Geoscience Atom Probe Facility, John de Laeter Centre, Curtin University, Perth, Australia
[c] Space Science and Technology Centre, Curtin University, Perth, Australia
[d] Timescales of Mineral Systems Group & John de Laeter Centre, Curtin University, Perth, Australia
[e] Department of Geology, University of Puerto Rico-Mayagüez, Mayagüez Puerto Rico, USA

ARTICLE INFO

Associate editor: Tsuyoshi Iizuka

Keywords:
Xenotime
Shock metamorphism
U-Pb geochronology
Geochronometers
Impact age

ABSTRACT

Shock-deformation microstructures in xenotime have been proposed to record diagnostic evidence for meteorite impacts. Evaluating the potential for impact-induced U-Pb age resetting of the various microstructures that form in shocked xenotime remains largely unexplored. In this study, we investigate the U-Pb systematics of shocked xenotime from three impact structures, including Vredefort (South Africa), Santa Fe (New Mexico, USA), and Araguainha (Brazil). Xenotime at these sites is found in shocked granite, impact melt rock, and as detrital grains, and preserves a range of impact-induced microstructures, including planar fractures, planar deformation bands, deformation twins, and polycrystalline neoblastic grains. Microstructures in xenotime were characterised by electron backscatter diffraction (EBSD) and then targeted for U-Pb geochronology. Secondary ion mass spectrometry (SIMS) and correlated atom probe tomography (APT) were used to determine age and element mobility mechanisms at micrometer- to nanometer-scale. At the precision of SIMS spots, grain areas characterised by lattice deformation microstructures do not show evidence of U-Pb system resetting. In contrast, some grains with neoblastic textures were found to yield impact ages, with U-Pb disturbance correlating to the extent of grain recrystallisation. The APT data showed nanoscale compositional heterogeneities in the form of Pb*-Ca enriched clusters, dislocations arrays, and grain boundaries, the latter with higher concentration of trace elements such as Si, Mg, Ca, Na, Cl, and Al. Combining microstructural, geochronological and nanoscale characterisation, this study demonstrates that neoblastic microstructures can yield accurate impact ages. Shocked xenotime with neoblastic texture is the most reliable geochronometer for dating impact events.

1. Introduction

Impact events are important in Earth's dynamic history, ranging from the hypothesis of triggering plate tectonics and consequent formation of lithospheric crust to promoting the evolution of life (Schulte et al., 2010; O'Neill et al., 2017; Osinski et al., 2020). To date, there are ~200 confirmed terrestrial impact structures (Earth impact database; Kenkmann, 2021; Osinski et al., 2022), yet less than 10 % have been accurately dated with a precision better than ±2 % (Jourdan et al., 2009, 2012; Schmieder and Kring, 2020). Dating an impact event is not trivial, as the amount of available geochronometers capable of providing precise impact ages are limited (McGregor et al., 2021). In addition, appropriate material for accurate dating is not always readily available because of erosion and/or post-impact processes which can reset the chemistry of accessory mineral geochronometers (e.g., Kamo et al., 1996). A common method for precise impact dating is based on the U-Pb system of accessory minerals such as zircon, monazite, apatite, titanite, and baddeleyite which can be targeted to specific microstructural domains (Hodych and Dunning, 1992; Darling et al., 2016; Erickson et al., 2017, 2020; Papapavlou et al., 2018; McGregor et al., 2018, 2019, 2020; Timms et al., 2020; Kenny et al., 2021).

Shock metamorphism occurs during meteoritic impact and involves

* Corresponding author at: School of Earth and Planetary Sciences, Curtin University, Perth, Australia.
E-mail address: denis.fougerouse@curtin.edu.au (D. Fougerouse).

https://doi.org/10.1016/j.gca.2024.04.017
Received 6 July 2023; Accepted 10 April 2024
Available online 15 April 2024

the formation of short-pulse, high-dynamic pressure, and high temperature that collectively cause instantaneous high strain damage to mineral structures within impacted bedrock. At microscale, shock metamorphism manifests as deformation microstructures that are diagnostic of impact processes (Langenhorst and Deutsch, 2012). For example, planar deformation features (PDF) in quartz, high pressure polymorphs (e.g., coesite, stishovite, reidite), and deformation twins (e.g., {1 1 2} twins in zircon) are interpreted as expressions of shock metamorphism (Langenhorst and Deutsch, 2012; Timms et al., 2017; Cavosie et al., 2021). The formation of certain microstructures has been shown to reset U-Pb geochronometers; for example, recrystallised polycrystalline aggregate (granular) zircon from impact sites can provide precise impact ages (Gibson et al., 1997; Moser, 1997; Cavosie et al., 2015; Kenny et al., 2021). However, granular zircon are susceptible to partial resetting during the impact, post-impact Pb-loss or Pb-gain, which can result in ages that are either older or younger than the impact event (Kamo et al., 1996, 2011; Tohver et al., 2012; Schmieder et al., 2015, 2019; McGregor et al., 2019, 2020). In monazite, granular domains and deformation twins have also been shown to yield impact ages (Erickson et al., 2017, 2020; Fougerouse et al., 2021a). However, monazite is also susceptible to age resetting (Williams et al., 2011). Apatite can yield impact ages, but typically has low actinide concentrations (<100 ppm U), and a high proportion of common Pb (from a few % to nearly 100 %; Chew et al., 2014; Kirkland et al., 2018). The U-Pb response of apatite to impact modification appears to be less controlled by microstructures compared to other accessory minerals, and more dependent on the textural setting of the grain (McGregor et al., 2018, 2020, 2021). Recrystallised polycrystalline neoblastic domains in titanite have been reported from several impact environments (e.g., Timms et al., 2020), however granular titanite does not always record impact age resetting (Cavosie et al., 2022, and references within).

Xenotime ([Y, HREE]PO_4) is a common accessory mineral in igneous rocks, in low- to high-grade metamorphic rocks, as well as a product of hydrothermal mineralisation, and as both a detrital and diagenetic phase in sedimentary rocks (Van Emden et al., 1997; McNaughton et al., 1999; Brown et al., 2002; Spear and Pyle, 2002; Rasmussen, 2005; Vallini et al., 2005; Aleinikoff et al., 2012; Li et al., 2013). Even though xenotime contains significant U and Th (up to 1000 s ppm), it is resistant to radiation damage, and metamictisation is rare (Harrison et al., 2002). During growth, xenotime incorporates negligible amounts of common Pb, and Pb diffusion is slower in xenotime than in other accessory phases such as monazite and zircon (Cherniak, 2006, 2010). Therefore, xenotime is considered to be a robust U-Pb geochronometer (Rasmussen, 2005; Hetherington et al., 2008; McNaughton and Rasmussen, 2018).

Xenotime has been shown to form similar shock deformation microstructures to those found in zircon, including planar fractures (PF), planar deformation bands (PDB), {1 1 2} deformation twin lamellae, recrystallisation to polycrystalline neoblastic domains (granular), and broad regions of crystal-plastic deformation (Cavosie et al., 2016a, 2021; Cox et al., 2021). Cavosie et al. (2021) combined in-situ U-Pb and microstructural investigation of PDB- and shock-twin-bearing xenotime grain from the Vredefort impact structure and concluded that no impact-age resetting is associated with either {1 1 2} twins or PDB. However, these workers did report evidence for a younger (post-impact) thermal event that caused Pb-loss recorded by a lower concordia intercept (Cavosie et al., 2021).

In this study, the microstructures of shocked xenotime grains from three impact structures including Vredefort (South Africa), Santa Fe (USA), and Araguainha (Brazil) were analysed. The aim of this investigation is to 1) characterise shock deformation microstructures in xenotime from different crater environments (where known), 2) evaluate the U-Pb response of the different shock microstructures in xenotime to assess which, if any, yield impact ages, and 3) determine mechanisms responsible for trace element mobility during shock-induced crystal-plastic deformation.

2. Geological settings and sample descriptions

2.1. Vredefort impact structure, South Africa

The Vredefort impact structure is located on the Kaapvaal Craton in South Africa and has been dated at 2020 ± 3 Ma using both zircon and monazite U-Pb geochronology (Kamo et al., 1996; Gibson et al., 1997; Moser, 1997; Erickson et al., 2017). With an original estimated diameter of ~300 km, the Vredefort impact structure is the largest recognised on Earth and is exposed as a ~90 km wide structure representing the eroded central uplift (Grieve and Therriault, 2000) (Fig. 1a). The core comprises ca. 3.1 Ga Archean granitoid gneissic rocks (~45 km wide) subdivided into an inner core of granulite facies leucogranitic gneiss (Inlandsee leucogranofels) and an outer core of amphibolite facies granodioritic to tonalitic gneiss (Outer granitoid gneiss). The core is surrounded by a 15–20 km collar of overturned strata comprising 3.07–2.02 Ga supracrustal sequences of the Dominion Group and the Witwatersrand, Ventersdorp, and Transvaal supergroups, with metamorphic grade transitioning from mid-amphibolite facies in the inner collar to greenschist facies in the outer collar (Kamo et al., 1996; Gibson et al., 1997, 1998; Moser, 1997).

The Vredefort shocked xenotime grain studied here is a detrital grain collected from a pavement of Permian tillite (sample 14DG14, 26°53′23.1″ S 27°24′23.0″ E) exposed in the outer core (Fig. 1a). The sampling site is located between the 10 and 15 GPa isobars defined by PDF in quartz (Gibson and Reimold, 2005); bedrock at this location is dominated by shocked granitoid and pseudotachylitic breccia. The host rock of the detrital shocked xenotime grain is not known; given its size, the grain is assumed to have an igneous origin.

2.2. Santa Fe impact structure, USA

The Santa Fe impact structure is located in the southern Sangre de Cristo Mountains, ~8 km northeast of Santa Fe, New Mexico, USA (Fackelman et al., 2008; Montalvo et al., 2019). Shatter cones and shocked quartz provided the initial evidence of an impact event (Fackelman et al., 2008, Fig. 1b). The shocked rocks that define the Santa Fe structure comprise a km-sized block that is fault-bound to the east and west (Montalvo et al., 2019). Rocks in the area are regionally metamorphosed gneissic granitoids and biotite granite, which are interlayered with amphibolite and metasedimentary rocks (Bauer and Ralser, 1995; Read et al., 2000; Bauer et al., 1996). In the area, there is no geomorphological or geophysical evidence of an impact structure, likely due to post-impact tectonic activity and erosion (Fackelman et al., 2008; Cavosie et al., 2016a; Montalvo et al., 2019). Estimates of crater diameter range from ~6 to 13 km based on shatter cone distribution and the presence of detrital shocked zircon in local drainages (Fackelman et al., 2008; Montalvo et al., 2019). The age of the Santa Fe impact event remains poorly constrained. A maximum impact age of 1472 ± 35 Ma is based on U-Pb analysis of a detrital shock-twinned zircon, with the age interpreted to represent igneous crystallisation (Montalvo et al., 2019). The minimum impact age of c. 350 Ma is based on undeformed Palaeozoic sedimentary rocks (Madera Group) overlying basement granitoids (Fackelman et al., 2008; Montalvo et al., 2019). Pressure estimates for exposed rocks in the area are up to 20 GPa based on PDF in quartz, shock-twinned zircon, and the abundance of shatter cones (Fackelman et al., 2008; Cavosie et al., 2016a; Montalvo et al., 2019).

Three Santa Fe shocked xenotime grains were studied (SFx3, SFx4, SFx5), and were all identified in one thin section. The host rock is a shatter cone of granitoid (sample 14NM10A, 35°43′35.6″N 105°51′26.9″W) mainly composed of alkali feldspar with minor quartz, plagioclase, muscovite, chlorite, biotite, and opaque minerals. Shock microstructures and the petrographic context of the three grains were previously described; their igneous origin is thus well-established (see Cavosie et al., 2016a) (Fig. 1b).

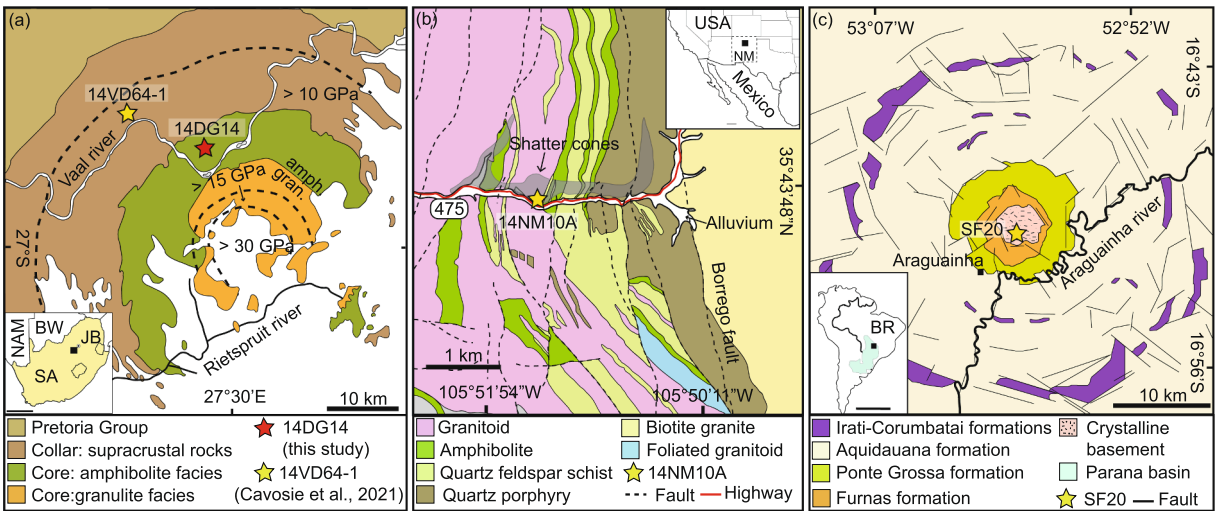

Fig. 1. Simplified geological maps of the three impact structures with sample locations. (a) The central uplift of the Vredefort dome, South Africa (modified after Cavosie et al. (2010)) with inset showing the location in South Africa (SA – South Africa, JB – Johannesburg, NAM – Namibia, BW – Botswana). (b) Map showing shocked rocks that define the Santa Fe impact structure (modified after Bauer et al. (1996) and Montalvo et al. (2019)), with inset showing the location of Santa Fe impact structure in New Mexico (NM – New Mexico). (c) Map of the Araguainha impact crater (modified after (Lana et al., 2008)) with inset showing location of Araguainha impact structure in Brazil.

2.3. Araguainha impact structure, Brazil

The Araguainha impact structure is located in the northern Paraná Basin of central Brazil, and is the best-exposed complex impact structure in South America (Tohver et al., 2012). The structure is ~40 km in diameter, with a 10 km wide central uplift, annular ring features, and a rim defined by radial and concentric faults (Lana et al., 2007). The central uplift comprises Cambrian alkali granite basement, which is crosscut by pseudotachylitic breccia and surrounded by thick (~1500–1800 m) Devonian to Permian sedimentary rocks in the collar (Lana et al., 2007; Lana et al., 2008; Tohver et al., 2012). The impact exposed the Araguainha granitoid, a pink coarse-grained monzo- to syenogranite, with a crystallisation age of 512 ± 11 Ma (Tohver et al., 2012). Shatter cones, melt rocks, and breccias are preserved in the central uplift, even though erosion has removed much of the crater fill (Engelhardt et al., 1992; Lana et al., 2008). Multiple studies have reported ages ranging from 260 to 250 Ma for the Araguainha impact event. A study of several different impactites combined the results of U-Pb and Th-Pb dating of zircon and monazite, and $^{40}Ar/^{39}Ar$ of melt inclusions, to yield an impact age of 254.7 ± 2.5 Ma (Tohver et al., 2012). Granular monazite from a sedimentary rock-derived impact melt rock yielded an impact age of ~260 Ma (Erickson et al., 2017). Granular zircon from a different sedimentary rock-derived impact melt rock yielded an impact age of 251.5 ± 2.9 Ma (Hauser et al., 2019).

The three Araguainha shocked xenotime grains (X1, X2 and X3) studied here are from an impact melt rock (sample SF20) derived from a sedimentary rock located in the core of the impact structure (16°49′45.3″S 52°59′16.8″W, Fig. 1c). The grains were identified in a heavy mineral concentrate, so their petrographic context is unknown. Given the protolith of the impact melt rock, the xenotime grains are assumed to be detrital grains that likely have an igneous origin.

3. Methods

3.1. Sample mounting

Vredefort xenotime 14DG14 was mounted in epoxy. The three Santa Fe grains were extracted from a thin section and re-mounted in epoxy separately. The three Araguainha xenotime grains were mounted in epoxy.

3.2. Scanning electron microscope-electron backscatter diffraction (SEM-EBSD)

Secondary electron (SE) images, backscattered electron (BSE) images, and EBSD analyses were acquired using TESCAN Clara and TESCAN Mira3 field emission gun scanning electron microscopes (FEG-SEM) housed in the John de Laeter Centre (JdLC) at Curtin University. For the Vredefort and Araguainha samples, EBSD analyses were done using a TESCAN Mira3 SEM, and the Santa Fe grains were analysed with a TESCAN Clara SEM; both instruments are equipped with Oxford Instruments Symmetry EBSD detectors. The EBSD conditions were similar for all samples, and generally follow methods described in Cavosie et al., 2016a and 2021 (Supplementary Table 1). In brief, all measurements used a 20 kV accelerating voltage, ~20–25 mm working distance, a 1–2nA beam current, and a 70° specimen tilt, with pixel sizes for maps ranging from 60 to 100 nm. EBSD maps were collected with the xenotime (Y) match unit from the Inorganic Crystal Structure Database (ICSD) based on structural data from Ni et al. (1995). The EBSD data were collected with the Oxford Instruments acquisition program AZtec, and post-processed using the software AZtecCrystal (v. 2.1). The EBSD maps used include band contrast (BC), which shows the quality of diffraction pattern; brighter areas are generally considered to be more crystalline than darker areas. Orientation maps with an inverse pole figure (IPF) color scheme show variations in crystallographic orientation, and are useful for resolving crystal-plastic deformation, twin lamellae, and neoblasts. Pole figures are all equal area lower hemisphere projections in the sample reference frame. The Grain Reference Orientation Deviation (GROD) angle map shows misorientation at any given point with respect to the average orientation of the grain. Texture component (TC) maps show the relative misorientation across a grain relative to a user-specified reference point.

3.3. Sensitive high resolution ion microprobe (SHRIMP) and Electron probe micro analyser (EPMA)

The U-Pb geochronology data were acquired in two sessions in January (Santa Fe and Araguainha) and March (Vredefort) 2022 at the JdLC using a SHRIMP II secondary ion mass spectrometer (SIMS). Xenotime standard MG-1 ($^{206}Pb^*/^{238}U$ age = 489.96 ± 0.54 Ma; $^{207}Pb^*/^{206}Pb^*$ age = 491.8 ± 1.2 Ma; U = ~900 ppm; Th = ~800 ppm) was used as the primary reference material. The standards z6413

($^{206}Pb^*/^{238}U$ age = 993.83 ± 0.74 Ma; $^{207}Pb^*/^{206}Pb^*$ age = 996.64 ± 0.82 Ma; U = ~10,000–20,000 ppm; Th = 1500–4000 ppm) and Y1 ($^{207}Pb^*/^{206}Pb^*$ age = 948 ± 5 Ma; U = ~8,000–25,000; Th = 3,500–10,000) were used as secondary reference materials (Fletcher et al., 2000, 2004). The reference materials were located on an adjacent mount to the unknowns in the SHRIMP, and both mounts were cleaned and gold-coated prior to each session. A spot size of ~10 × 7 μm was produced by passing the primary O^{2-} ion beam through a ~30 μm Kohler aperture. Each analysis consisted of six scans, including a nine peak run table of $^{194}Y_2O^+$, $^{204}Pb^+$, background ($^{204}Pb^+$ + 0.0145 AMU offset), $^{206}Pb^+$, $^{207}Pb^+$, $^{208}Pb^+$, $^{238}U^+$, $^{248}ThO^+$ and $^{254}UO^+$ (Fletcher et al., 2004). A retardation lens was used in front of the secondary ion collector to maximise the abundance sensitivity and eliminate scattered ions (Fletcher et al., 2000).

Calibrating Pb/U and Th/U ratios was done using SQUID3 software, using fixed (slope = 2) robust regressions through $\ln(^{206}Pb^+/^{238}U^+)$ vs $\ln(^{254}UO^+/^{238}U^+)$ for MG-1 (Bodorkos et al., 2020). The calibration constants obtained for the January and March sessions were 0.0052 ± 1.1 % (1σ, MSWD = 1.4, p = 0.11) and 0.0076 ± 0.9 % (1σ, MSWD = 1.3, p = 0.17), respectively. A common Pb correction was determined using contemporaneous Pb compositions of Stacey and Kramers (1975).

U-Pb dating of xenotime by SIMS requires a correction for matrix effect, particularly for different REE-U-Th abundances between the standard and samples (Fletcher et al., 2004). The U and Th concentrations were determined directly from the SHRIMP data and the ΣREE values were determined using a JEOL JXA-8530F Electron Probe Microanalyser (EPMA) (Supplementary Table 2) at the Centre for Microscopy, Characterisation and Analysis at the University of Western Australia. A take-off angle of 40° and beam energy of 25 keV were used during analysis. The EMPA beam current was 100 nA for both calibration and unknown sample measurements. The unknowns were acquired using the Probe for EPMA© 257 software package (Probe Software®). A selection of in-house silicates, Drake and Weill glasses, and USNM REE phosphates from the Smithsonian Institute were used as standards for instrumental calibration. During the analytical sessions, when matrix-corrected using U, Th and ∑REE concentrations, z6413 and Y1 yield $^{206}Pb^*/^{238}U$ and $^{207}Pb^*/^{206}Pb^*$ weighted mean ages within 2 s.d. of published values. Age calculations and plots were made with Isoplot 4.15 (Ludwig, 2012) and IsoplotR (Vermeesch, 2018).

3.4. Atom probe tomography (APT)

Needle-shaped specimens for atom probe tomography were prepared using a TESCAN Lyra3 Ga + focused ion beam with SEM (FIB-SEM) at the JdLC, Curtin University, and were accurately targeted using Pt fiducials (Rickard et al., 2020). For milling and shaping of the specimens the FIB was operated at a 30 kV accelerating voltage, followed by a 2 kV cleaning procedure for final polishing of the specimen. A total of 22 xenotime APT specimens were extracted from grains representative of each impact structure.

The specimens were analysed using a CAMECA local electrode atom probe (LEAP) 4000X HR at the Geoscience Atom Probe Facility, JdLC, Curtin University. The instrument was operated in laser-assisted mode using a UV laser (λ = 355 nm). For each analysis, analytical parameters such as temperature, detection rate, laser pulse energy and laser pulse frequency were kept constant at 60 K, 1 %, 200 pJ and 125 kHz respectively. The mass-to-charge spectrum was reconstructed to 3D data using AP Suite 6 software. For the 3D reconstruction, voltage-based models were applied. The detector efficiency was set at 36 %, k-factor at 3.3, image compression factor at 1.65, atomic volume computed at 0.01190 nm^3/atom for xenotime, and the field evaporation estimated at 28.98 V/nm as determined empirically (Fougerouse et al., 2021c).

In the 3D reconstruction, cluster identification was obtained by the maximum separation method (MSM; Williams et al., 2013) with the following parameters: dmax (maximum cluster ion separation) – 1.5 nm, O (order) – 1, N (number of chemical species) – 30, L (cluster detection envelope parameter) and E (cluster detection erosion distance) both – 0.75 nm.

The isotopic composition of U and Pb is measured from a narrow 0.1 Da range on the $^{206}Pb^{++}$, $^{207}Pb^{++}$, and $^{238}UO_2^{++}$ peaks and corrected for background. The background was estimated using a peak-free region (1 Da) adjacent to each peak (constant background estimation method, Joseph et al., 2021). For U-Pb dates, the $^{206}Pb/^{238}U$ ratio is calculated using the fractionation correction method, between the ratio of UO_2^{++}/UO^{++} and $^{206}Pb^{++}/^{238}UO_2^{++}$ for each analysis (Joseph et al., 2021). The $^{207}Pb/^{206}Pb$ dates were calculated using a variable background correction method (Joseph et al., 2021).

4. Results

Results of BSE, EBSD, SHRIMP and APT analyses of shocked xenotime are summarised below for the Vredefort grain, and three grains each from the Santa Fe and Araguainha impact structures.

4.1. Microstructural characterisation of shocked xenotime

4.1.1. Vredefort impact structure

Xenotime grain 14DG14 from Vredefort is a ca. 300 × 170 μm round-shaped crystal. In BSE, four distinct directions of PF are visible (Fig. 2a). Backscattered electron imaging reveals lower intensity, slightly darker patches heterogeneously distributed throughout the grain. EBSD orientation mapping shows the presence of low angle boundaries (<10° misorientation), PDB, deformation twins, and localised neoblastic textures (Fig. 2b-d). The neoblasts occur as isolated rounded grains with well-defined discreate grain boundaries, rather than forming a connected polycrystalline domain. Three different sets of deformation twin lamellae along {1 1 2} were identified (t1, t2, t3), all defined by a 65° disorientation about the host ⟨1 1 0⟩ (Fig. 2b,f) and a shared {1 1 2} direction between host and twin. The t1 twin set is the most dominant in the grain, consisting of 11 discrete lamellae; the t2 and t3 twins contain fewer lamellae. Twin lamellae are generally < 1 μm in width, except for some t1 twin lamellae, which have apparent widths up to ~1.6 μm. The three twin directions coincide with the directions of planar fractures (PF2-4) in the grain (Fig. 2a,b). Individual twin lamellae occur in segments as long as ~30 μm but are otherwise generally discontinuous. The {1 1 2} twin in t3 orientation consists of a single lamella that is segmented into a series of 2 to 3 μm long lamellae, some of which deviate from the canonical 65°/⟨1 1 0⟩ twin disorientation (Fig. 2e). The individual segments define misorientations close to, but different from, the {1 1 2} twin, including 72°/⟨3 4 2⟩, 68°/⟨2 3 2⟩, 70°/⟨3 4 1⟩, and 70°/⟨3 4 0⟩ (Fig. 2e,f).

A set of low angle boundaries is observed parallel to the t1 and t2 twin directions (Fig. 2b,c), and cumulative strain up to 12° is present across the grain. Maximum degree of crystalline distortion is localised at the edges of the grain and in proximity to PF2 and PF3 (Fig. 2c). PDBs are present, and dominantly parallel to the t1 and t2 {1 1 2} twins, with relatively sharp boundaries and typically < 3° of misorientation from the host. Broader PDB with diffuse boundaries are found sub-parallel to the t3 twin, and preserve cumulative misorientations up to ~12° from the host (Fig. 2c). Isolated neoblasts (up to 5 μm in diameter) are present along PF1 and some have an orientation similar to the t1 twin, whereas others appear randomly oriented (Fig. 2d,f).

4.1.2. Santa Fe impact structure

Microstructures in the three analysed xenotime grains from the Santa Fe impact structure (SFx3, SFx4, SFx5) are similar to those previously described by Cavosie et al., (2016a). All of the grains contain PF, areas with conspicuous lattice misorientation, PDB, and two of the grains contain {1 1 2} twins. Planar fractures occur in one orientation in grain SFx4, and three orientations in grains SFx3 and SFx5 (Fig. 3a,b,c). Grain SFx4 contains a single {1 1 2} twin lamella, whereas SFx5 contains three sets of twins (Fig. 3e,f,g); in all cases, the twin orientations coincide with

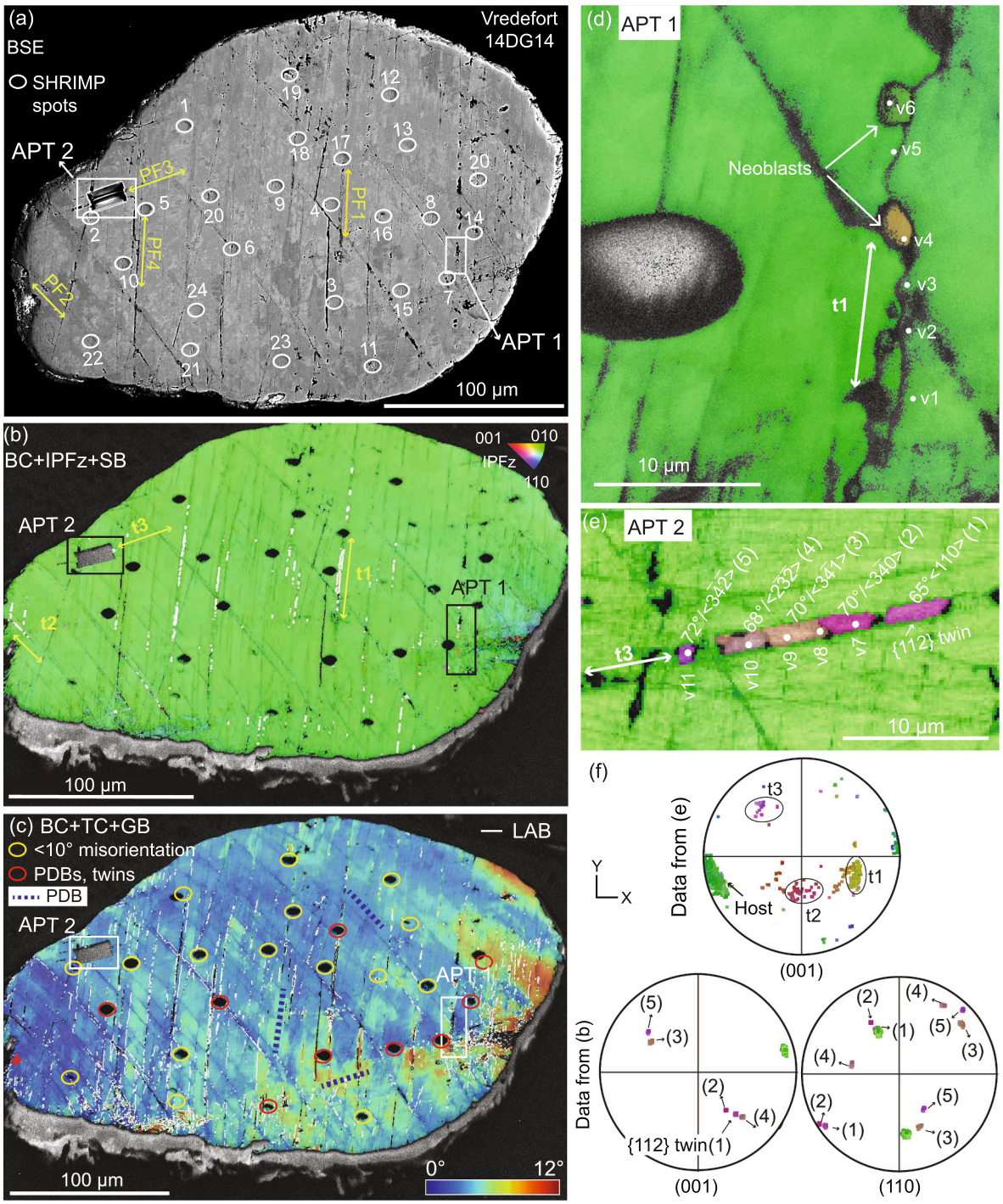

Fig. 2. Microstructures of Vredefort xenotime grain 14DG14. (a) Backscattered electron (BSE) image. Four orientations of planar fractures (PF1 – PF4) are visible. SHRIMP spots and atom probe sample locations are indicated. (b) Electron backscatter diffraction (EBSD) grain orientation map (inverse pole figure, z projection [IPFz]). Deformation features are indicated, including deformation twin lamellae (t1-t3) parallel to planar fractures (PF). (c) Texture component map showing low angle boundaries (<10° in white color), planar deformation bands (PDB) in three directions (dark blue dashed line). The grain shows up to 12° of misorientation from the reference point (red cross, left side). SHRIMP spots targeting PDB and twins are shown in red, and yellow ellipses shows SHRIMP spots targeted the areas in the grain with < 10° of misorientation. (d) Inverse pole figure (IPFz) map showing location of atom probe sample APT 1, which targeted and area with recrystallised neoblasts. (e) Inverse pole figure map showing location of atom probe sample APT 2, which targeted a segmented twin lamella (t3). Four segments define disorientations close to, but different from, the {1 1 2} twin orientation, including 72°/⟨3 4 2⟩, 68°/⟨2 3 2⟩, 70°/⟨3 4 1⟩, and 70°/⟨3 4 0⟩; only one segment locally records the {1 1 2} twin direction (65°/⟨1 1 0⟩). (f) Pole figures showing twin and host relations from (b) and (e).

the traces of PF on the polished surface. In grain SFx5 the t1 twins are the dominant set, with apparent lamellae widths up to 270 nm. Twins in sets t2 (subparallel to t1) and t3 consist of thin lamellae that are generally only ~50 nm (one pixel) in apparent width.

4.1.3. *Araguainha impact structure*

Xenotime grains X1, X2 and X3 from Araguainha are subhedral to anhedral rounded grains that range from 50 to 200 µm in length (Fig. 4a, bc). The EBSD BC images show that all three are partially to fully polycrystalline. Orientation maps for grain X1 shows a mixture of highly

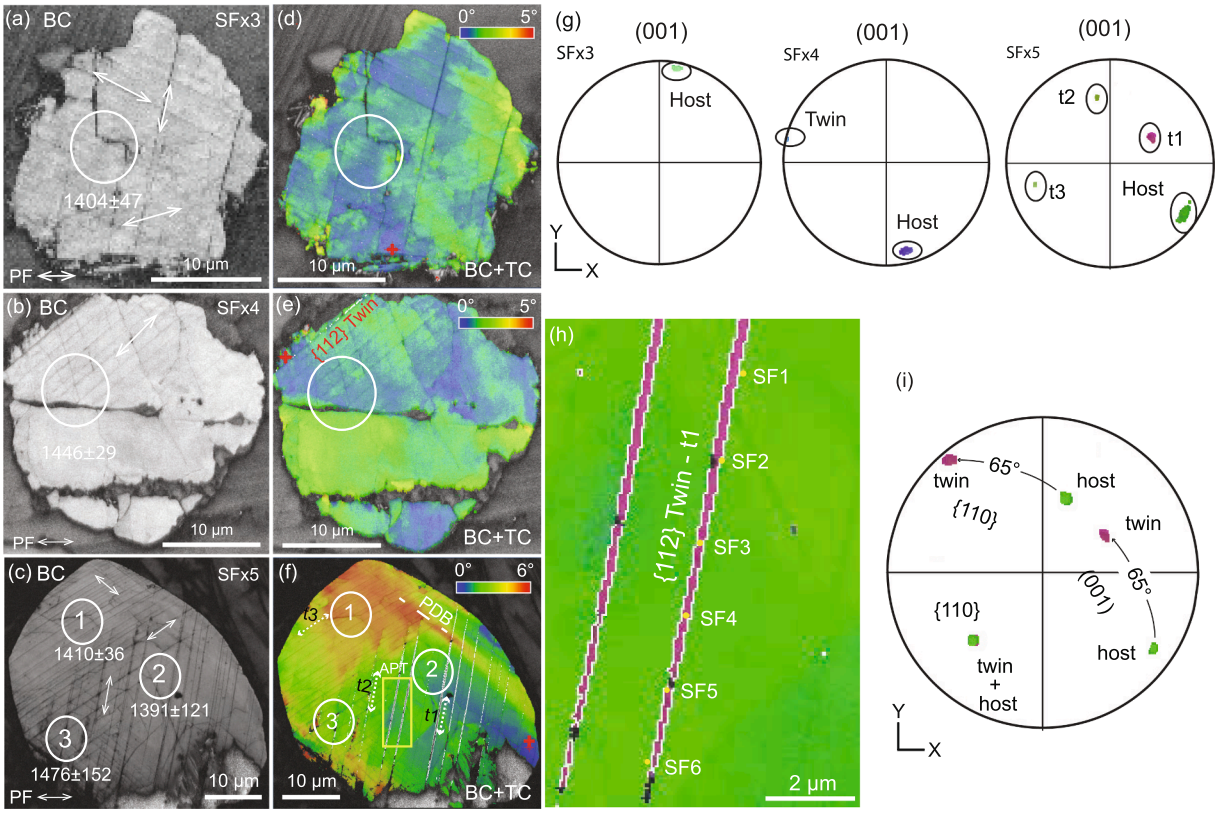

Fig. 3. Microstructures of Santa Fe xenotime grains. (a), (b) and (c). Band contrast (BC) images showing directions of planar fractures (indicated by arrows). The SHRIMP spots are indicated, along with ages in Ma. (d), (e) and (f). Texture component (TC) maps showing relative misorientation from a reference point (red cross). (d) Grain SFx3 showing up to 5° misorientation. (e) Grain SFx4 showing one {1 1 2} twin lamella and up to 5° misorientation. (f) Grain SFx5 showing three sets of {1 1 2} twin lamellae (t1, t2, t3), up to 6° of misorientation, and planar deformation band (PDB). (g) Pole figures of (0 0 1) showing host-twin relationships for grains SFx3, SFx4 and SFx5 (lower-hemisphere, equal-area projection). (h) Location of atom probe samples in grain SFx5 (see inset in (f). (i) Pole figure of data shown in (h), illustrating the {1 1 2} twin-host orientation relationship.

strained host and neoblasts that are mostly equant and range in size from 2 to 15 μm (Fig. 4d). Neoblasts mostly occur along the margin of the grain, in clusters within the grain, and along fractures, and define two main orientation populations in the pole figure; each cluster shows considerable orientation dispersion (Fig. 4d, pole figure). A more detailed examination of orientation data for grain X1 reveals that the host domain is largely preserved across the grain and records a cumulative misorientation of ~20° (Fig. 5a). Further, each neoblast orientation clusters preserves a systematic orientation relation with the host domain of 65°/⟨1 1 0⟩ and shares a {1 1 2} direction (Fig. 5b,c). The neoblast orientations preserve the same orientations as {1 1 2} twin lamellae, and are thus interpreted to represent recrystallised {1 1 2} twins.

EBSD orientation maps for grain X2 indicate that the grain internally consists of an aggregate of elongate neoblasts that define two main orientations. The dominant orientation is sub-parallel to the c-axis, whereas the smaller orientation cluster is nearly orthogonal to the main (Fig. 4e).

Orientation maps for grain X3 show a fully neoblastic aggregate of inequigranular grains, most of which have high-angle boundaries (Fig. 4c,f). Although there is considerable dispersion in orientations, the neoblasts appear to define two or more broad orientations, with an inner zone consisting of neoblasts with similar orientations and an outer zone of randomly oriented neoblasts (Fig. 4f, pole figure). No systematic orientation relations indicative of recrystallised {1 1 2} twins were detected in grains X2 or X3. Internally, the neoblasts are generally strain free, although a small number of neoblasts shows up to 15° internal misorientation; these are distributed mainly in the central portion of the grain, and probably represent less recrystallised relict host domains (Supplementary Fig. 1). In the GROD angle map, a lobate texture is seen generally along grain boundaries, in which a low strain neoblast has grown into a neoblast with high misorientation (Fig. 4h). This particular type of grain boundary was targeted for nanoscale analysis by APT.

4.2. SIMS U-Pb geochronology

A total of 24 SHRIMP spots (Fig. 2a and 6a) were made on Vredefort xenotime 14DG14. The U concentration varies from 1200 to 1900 ppm, with a Th/U ratio from 1.8 to 2.4 (Table 1). The upper concordia intercept yields an age of 3136 ± 110 Ma (2σ), and the lower concordia intercept yields an age of 1803 ± 280 Ma (2σ). No correlation was observed between actinide concentration and BSE contrast, or between degree of crystal misorientation and U-Pb discordance. Spots that overlapped PDB and/or {1 1 2} twins show minor variations in $^{207}Pb^*/^{206}Pb^*$ age but do not define unique regions of the discordia regression (Fig. 6a). No analyses plot near the 3136 Ma upper intercept; the oldest five near-concordant analyses (spots 1, 13, 18, 20, and 24) yield a weighted mean $^{207}Pb^*/^{206}Pb^*$ age of 2938 ± 16 Ma (2σ, MSWD = 0.78, p = 0.53), and likely represent a minimum crystallisation age for the detrital grain. The lower intercept age of 1803 ± 280 is imprecise; it overlaps both the accepted impact age (2020 Ma, Kamo et al., 1996) and also a recently proposed hydrothermal event at ca. 1750 Ma (Cavosie et al., 2021).

Five SHRIMP spots on three xenotime grains from Santa Fe shocked granite sample 14NM10 yield concordant (or nearly so) analyses (Fig. 3a,b,c, and 6b). The U concentration varies from 4770 ppm (SFx4), to 5800 ppm (SFx3), and to 8000–11,200 ppm (SFx5) (Table 1). A $^{207}Pb^*/^{206}Pb^*$ weighted mean age for all analyses is 1427 ± 20 Ma (2σ,

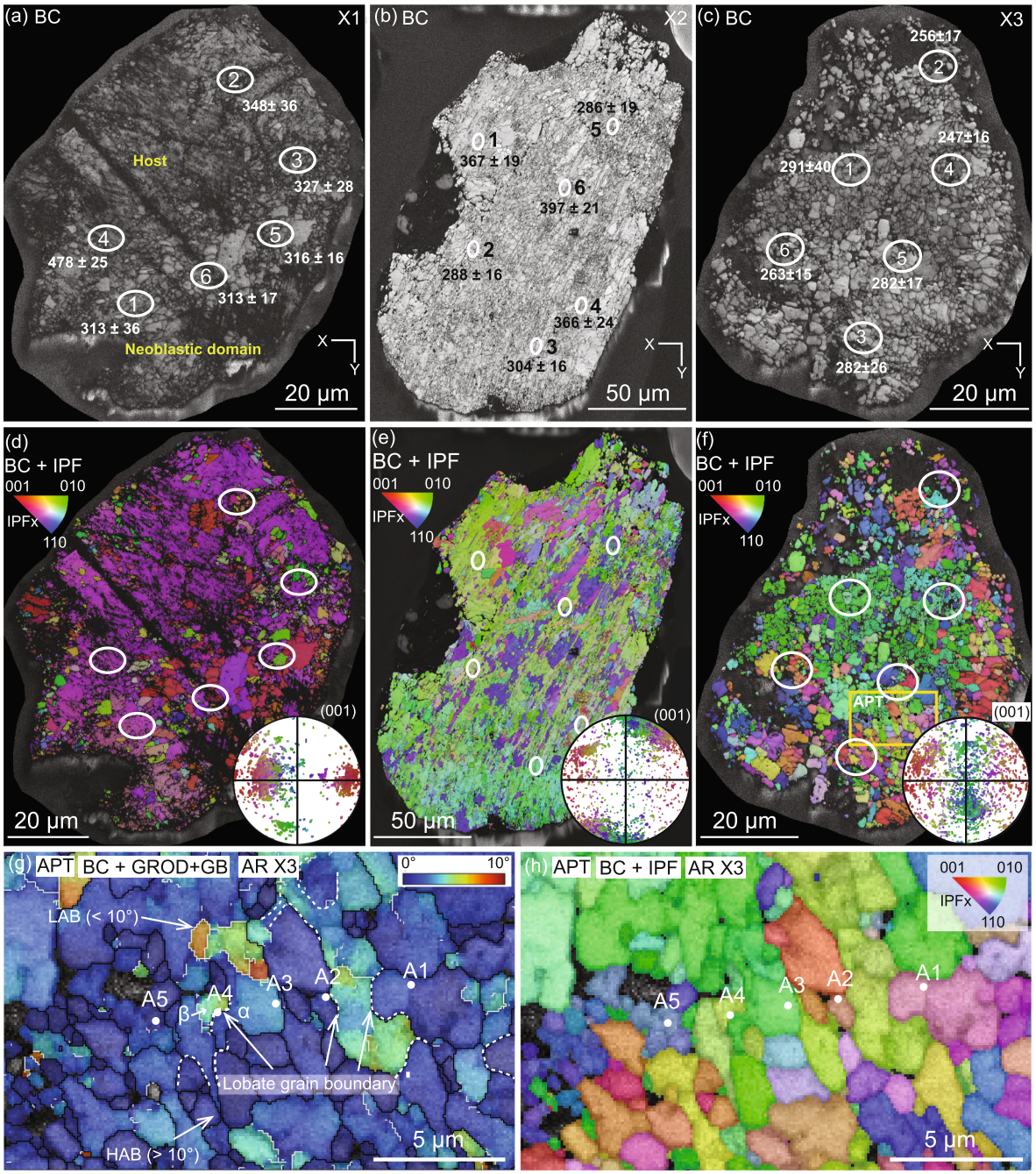

Fig. 4. Microstructures of three recrystallised xenotime grains from the Araguainha impact structure. (a), (b) and (c). EBSD band contrast (BC) maps with SHRIMP spots and U-Pb ages in Ma indicated. (d), (e) and (f). EBSD grain orientation maps (inverse pole figure, x projection [IPFx]) with insets showing orientation distribution of the recrystallised neoblasts from (001) pole figures (lower-hemisphere, equal-area projection). (g) Grain reference orientation deviation (GROD) angle map of the area shown in (f) showing up to 10° orientation deviation from the average orientation of the grain. Note the lobate texture between neoblasts at the A4 atom probe specimen location, in which the larger grain (α) with no misorientation is grown into grain with higher internal misorientation (β). Dashed lines represent contact between neoblasts showing lobate texture. (h) Close-up IPFx map showing location of atom probe samples from grain X3.

MSWD = 1.10, p = 0.36, n = 5).

A total of 18 SHRIMP spots were made on the three Araguainha xenotime grains, with six spots on each grain (Fig. 7a). The U concentrations vary from ~3600–7100 ppm (Table 1), and most analyses yield concordant ages ranging from ca. 475 to 250 Ma. For grain X1, five of six analyses overlap and yield a weighted mean $^{238}U/^{206}Pb$ age of 318 ± 10 Ma (2σ, MSWD = 0.92, p = 0.45, n = 5); the sixth spot is conspicuously older and was not included in the age calculation (Fig. 7b). For grain X2, the six analyses yielded a bimodal age population (Fig. 7c). The three youngest analyses yield a weighted mean $^{238}U/^{206}Pb$ age of 293 ± 9 Ma (2 σ, MSWD = 1.5, p = 0.22, n = 3), whereas the three older analyses yield a weighted mean $^{238}U/^{206}Pb$ age of 378.5 ± 12 Ma (2σ, MSWD = 2.5, p = 0.085, n = 3). Grain X3 yielded the youngest age population. The six analyses from grain X3 define a discordia array defined by a mixture of common and radiogenic Pb (Fig. 7d). A regression through all six analyses yields a lower intercept age of 255 ± 11 Ma (2σ, MSWD = 1.9, p = 0.11, n = 6) which is interpreted as the time of neoblast formation. The upper concordia intercept indicates a $^{207}Pb/^{206}Pb$ ratio of 0.42 ± 0.32, which is interpreted to represent the composition of common Pb present when the neoblasts formed.

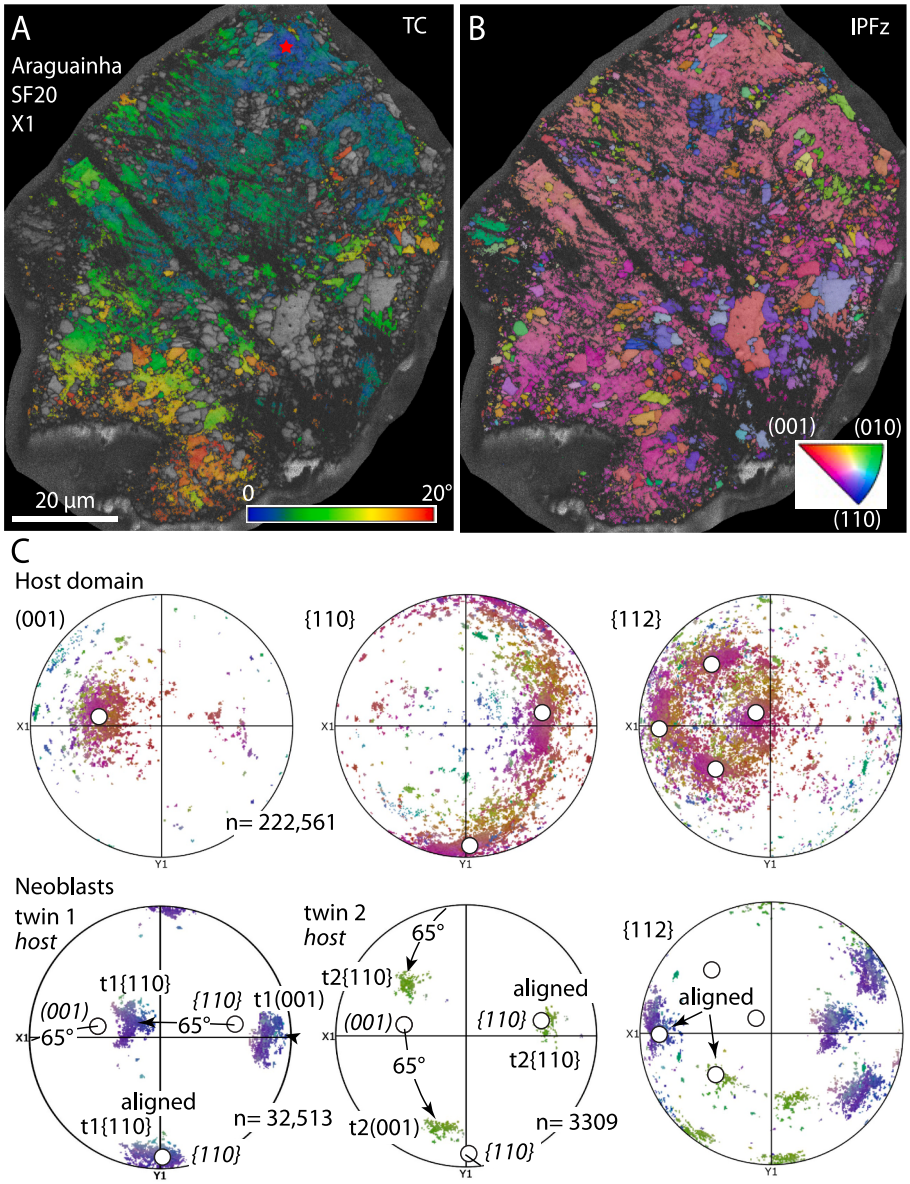

Fig. 5. (a) Texture component map of Araguainha grain X3 showing cumulative misorientation of ~20° in the remnant host domain. (b) Orientation map (IPFz) of grain X3. (c) Pole figures of data from (b) showing orientation relationships between the host domain and neoblasts. The white circles indicate the highest density of host domain orientations based on contouring. Each neoblast cluster has a 65°/⟨1 1 0⟩ relation about the host domain, and shares a {1 1 2} direction with the host.

4.3. Nanoscale characterisation

Nanoscale characterisation of deformation microstructures in xenotime was conducted with APT, targeting deformation twins (Vredefort and Santa Fe) and neoblastic domains (Vredefort and Araguainha. A total of 22 APT specimens were prepared and 16 ran successfully (73 % success rate). The survivability of APT specimens of shocked xenotime during atom probe analyses was thus higher than that for APT specimens of shocked zircon (12 % success rate) (Montalvo et al., 2019; Montalvo, 2020). No ^{204}Pb peak was detected in the mass spectra from any of the xenotime specimens.

4.3.1. Vredefort xenotime (grain 14DG14)

Eleven APT specimens were prepared from the Vredefort xenotime grain, including six from individual neoblasts (APT 1 area) and five from the {1 1 2} twins (APT 2 area) (Fig. 2d,e). Seven of the eleven APT specimens ran successfully. Six of the seven APT specimens (2 from neoblasts and 2 from {1 1 2} twins) preserve trace element segregations (clusters) at nanoscale (Fig. 8a, Supplementary Fig. 2).

Five specimens from the highly strained domain of the grain (APT2 area) yielded more than 10 million ions each. Two specimens (V1 and V4) contain thirteen randomly distributed Ca and Pb*-rich nanoscale clusters that range in size from ~8 to 20 nm (Fig. 8a). The abundances of Ca, Pb, and Si are lower in the matrix and higher in the clusters (Ca: 0.04 vs. 7 at. %; Pb: 0.09 vs. 3.5 at. %; Si: 0.08 vs. 1.86 at. %). Specimen V4 contains clusters enriched in OH and Na, which defines a discontinuous linear feature diagonal to the long axis of the specimen. There are also clusters enriched in Al distributed randomly through the specimen and also along the linear feature. Chlorine is heterogeneously distributed; it forms clusters and also correlates to Ca distribution in the specimen (Fig. 8a). In specimen V5, a set of dislocations enriched in Si, Cl, Ca, Na, and Al is present in a planar domain that is nearly perpendicular to the long axis of the specimen (Supplementary Fig. 2). In specimen V3 a dislocation has elevated Ca and Si, and specimen V2 showed no heterogeneities (Supplementary Fig. 2).

The APT ^{207}Pb/^{206}Pb dates obtained from the whole specimen with

Table 1
Secondary ion mass spectrometry (SIMS) analyses of xenotime grains from vredefort, santa fe and araguainha.

Sample	Spot	U (ppm)[c]	Th (ppm)[c]	Th/U	$(^{238}U/^{206}Pb^*)^m$ ± 2 s.e.	$(^{207}Pb^*/^{206}Pb^*)^m$ ± 2 s.e.	$(^{206}Pb^*/^{238}U)^m$ Age (Ma) ± 2 s.e	$(^{207}Pb^*/^{206}Pb^*)^m$ Age (Ma) ± 2 s.e	Disc. (%)[e]
Vredefort	SA21.17	1526	3013	2.04	2.15712 ± 0.16745	0.19070 ± 0.00393	2455 ± 159	2747 ± 34	10.6
Vredefort	SA21.15	1575	3123	2.05	2.02645 ± 0.14927	0.19831 ± 0.00408	2586 ± 157	2812 ± 34	8.0
Vredefort	SA21.19	1452	3101	2.21	2.12106 ± 0.16735	0.19875 ± 0.00850	2490 ± 163	2815 ± 70	11.6
Vredefort	SA21.8	1468	3072	2.16	2.17691 ± 0.16262	0.19907 ± 0.00409	2437 ± 152	2818 ± 34	13.5
Vredefort	SA21.2	1253	2541	2.10	2.10418 ± 0.16027	0.20139 ± 0.00908	2507 ± 158	2837 ± 74	11.6
Vredefort	SA21.4	1552	3114	2.07	2.02541 ± 0.15211	0.20399 ± 0.00387	2587 ± 160	2858 ± 31	9.5
Vredefort	SA21.11	1383	2754	2.06	2.11159 ± 0.16120	0.20592 ± 0.00409	2499 ± 158	2873 ± 32	13.0
Vredefort	SA21.3	1915	3972	2.14	1.98892 ± 0.14246	0.20695 ± 0.00856	2626 ± 155	2881 ± 67	8.9
Vredefort	SA21.9	1470	2768	1.95	1.99836 ± 0.15231	0.20765 ± 0.00411	2616 ± 164	2887 ± 32	9.4
Vredefort	SA21.5	1404	2742	2.02	2.00211 ± 0.14788	0.20916 ± 0.00404	2612 ± 159	2898 ± 31	9.9
Vredefort	SA21.21	1701	3408	2.07	2.11564 ± 0.16173	0.21009 ± 0.01061	2495 ± 158	2906 ± 82	14.1
Vredefort	SA21.6	1786	3201	1.85	1.96111 ± 0.13748	0.21056 ± 0.00375	2656 ± 153	2909 ± 29	8.7
Vredefort	SA21.10	1449	2686	1.91	2.00088 ± 0.14837	0.21376 ± 0.00229	2613 ± 159	2934 ± 17	10.9
Vredefort	SA21.12	1214	2477	2.11	1.79750 ± 0.07452	0.22387 ± 0.00432	2851 ± 96	3008 ± 31	5.2
Vredefort	SA21.7	1689	3937	2.41	2.24135 ± 0.26679	0.17968 ± 0.00454	2378 ± 237	2649 ± 42	10.2
Vredefort	SA21.23	1715	3229	1.95	1.93471 ± 0.13430	0.20057 ± 0.00364	2686 ± 153	2830 ± 30	5.1
Vredefort	SA21.16	1698	3445	2.10	2.05245 ± 0.25412	0.20192 ± 0.00401	2559 ± 262	2841 ± 32	9.9
Vredefort	SA21.22	1614	3051	1.95	2.02117 ± 0.24952	0.20815 ± 0.00388	2591 ± 264	2890 ± 30	10.4
Vredefort	SA21.14	1321	2813	2.20	1.98030 ± 0.23122	0.20065 ± 0.03016	2635 ± 253	2831 ± 245	6.9
Vredefort	SA21.20	1574	3020	1.98	1.93593 ± 0.14818	0.20989 ± 0.00965	2685 ± 168	2904 ± 75	7.6
Vredefort	SA21.13	1365	2765	2.09	1.89704 ± 0.14480	0.21290 ± 0.00429	2729 ± 170	2927 ± 33	6.8
Vredefort	SA21.18	1379	2771	2.08	1.98621 ± 0.29713	0.21328 ± 0.00427	2629 ± 323	2930 ± 32	10.3
Vredefort	SA21.24	1842	3700	2.08	1.80869 ± 0.13076	0.21584 ± 0.00370	2837 ± 166	2949 ± 28	3.8
Vredefort	SA21.1	1647	3650	2.29	1.85969 ± 0.12888	0.21736 ± 0.00626	2774 ± 156	2961 ± 46	6.3
Santa Fe	SF-X5-1	11,219	4151	0.38	3.85350 ± 0.16709	0.08933 ± 0.00169	1487 ± 58	1410 ± 36	−5.5
Santa Fe	SF-X5-2	8131	3609	0.46	3.59455 ± 0.70963	0.08842 ± 0.00558	1582 ± 277	1391 ± 121	−13.8
Santa Fe	SF-X3	5845	1931	0.34	3.88719 ± 1.22613	0.08902 ± 0.00217	1476 ± 417	1404 ± 47	−5.1
Santa Fe	SF-X4	4770	2677	0.58	4.23618 ± 0.63767	0.09104 ± 0.00140	1366 ± 185	1446 ± 29	5.6
Santa Fe	SF-X5-3	10,480	6751	0.67	4.63713 ± 1.68627	0.09245 ± 0.00742	1259 ± 416	1476 ± 152	14.7
Araguainha	AR-X03.2	4318	7546	1.81	24.68074 ± 1.66143	0.06468 ± 0.00805	256 ± 17	763 ± 262	66.4
Araguainha	AR-X03.5	4855	4623	0.98	22.36557 ± 1.40492	0.07370 ± 0.00718	282 ± 17	1032 ± 197	72.7
Araguainha	AR-X03.3	6447	13,958	2.24	22.37416 ± 2.11984	0.10059 ± 0.01891	282 ± 26	1634 ± 349	82.8
Araguainha	AR-X02.5	4443	5362	1.25	22.02111 ± 1.45737	0.06525 ± 0.00786	286 ± 19	782 ± 253	63.4
Araguainha	AR-X01.3	5266	7511	1.47	19.20134 ± 1.69558	0.06377 ± 0.00443	327 ± 28	733 ± 147	55.4
Araguainha	AR-X01.2	6013	8606	1.48	18.05340 ± 1.91396	0.05642 ± 0.00201	348 ± 36	468 ± 79	25.7
Araguainha	AR-X02.1	4445	3140	0.73	17.06135 ± 0.93070	0.06008 ± 0.00473	367 ± 19	605 ± 170	39.3
Araguainha	AR-X03.4	4761	4929	1.07	25.58971 ± 1.64670	0.05455 ± 0.00614	247 ± 16	393 ± 253	37.1
Araguainha	AR-X03.6	5619	4443	0.82	23.99637 ± 1.43861	0.05485 ± 0.00610	263 ± 15	405 ± 249	35.1
Araguainha	AR-X03.1	4865	4658	0.99	21.66397 ± 3.01894	0.05696 ± 0.00596	291 ± 40	489 ± 231	40.5
Araguainha	AR-X02.2	4626	4388	0.98	21.91018 ± 1.22334	0.04760 ± 0.00845	288 ± 16	78 ± 422	−266.8
Araguainha	AR-X02.3	5324	3943	0.77	20.68957 ± 1.09997	0.05517 ± 0.00514	304 ± 16	418 ± 208	27.2
Araguainha	AR-X01.6	5355	4765	0.92	20.11042 ± 1.12048	0.05534 ± 0.01018	313 ± 17	425 ± 410	26.4
Araguainha	AR-X01.1	4841	3879	0.83	20.07831 ± 2.39512	0.05537 ± 0.00914	313 ± 36	426 ± 368	26.5
Araguainha	AR-X01.5	7147	9905	1.43	19.93420 ± 1.06757	0.05640 ± 0.00394	316 ± 16	467 ± 155	32.4
Araguainha	AR-X02.4	3607	2586	0.74	16.84912 ± 1.06443	0.05848 ± 0.02007	372 ± 23	547 ± 750	32.0
Araguainha	AR-X02.6	4082	3183	0.81	15.74079 ± 0.84631	0.05137 ± 0.00710	397 ± 21	256 ± 318	−54.8
Araguainha	AR-X01.4	5164	4447	0.89	12.98176 ± 0.69926	0.06172 ± 0.00728	478 ± 25	663 ± 253	27.9

Decay constants of Jaffey et al. (1971) used, $^{238}U/^{235}U = 137.818$ (Hiess et al., 2012). Uncertainties quoted without components related to systematic error unless otherwise stated.
Total extra systematic uncertainties. 206Pb/238U = 0.11 %, 207Pb/206Pb = 0.14 % (2σ).
Data corrected for common Pb using contemporaneous common Pb compositions from Stacey and Kramers (1975).
[c] Concentration uncertainty ~20 %.
[e] Discordance calculated as 100*([^{206}Pb-^{238}U age-^{207}Pb-^{206}Pb age]/^{207}Pb-^{206}Pb age).
[m] Matrix corrected values.

Ca-Pb* clusters are 3005 ± 547 Ma and 3101 ± 674 Ma (2σ) from V1 and V4 specimens respectively. The matrix, which excludes the Ca-Pb* clusters from specimens V1 and V4, yield $^{207}Pb/^{206}Pb$ dates of 2859 ± 618 Ma (V1) and 2519 ± 1088 Ma (V4) respectively. Other specimens are homogeneous in Ca and Pb distribution at nanoscale (no clusters) and yield $^{207}Pb/^{206}Pb$ dates of 2411 ± 777 Ma, 2591 ± 968 Ma, 2647 ± 780 Ma (2σ). The combined data from specimens V2, V3, and V5 yield a weighted mean average of 2647 ± 350 Ma (2σ, MSWD = 0.23, p = 0.92). The APT $^{206}Pb/^{238}U$ dates from the five whole specimens, including specimens containing Pb*-rich clusters (V1 to V5), range from 1450 ± 187 Ma to 1749 ± 286 Ma (2σ), with a weighted mean average age 1596 ± 93 Ma (MSWD = 1.12, p = 0.35, n = 5). The matrix $^{206}Pb/^{238}U$ dates from specimens with clusters (V1 and V4) yields 1539 ± 184 Ma and 1611 ± 276 Ma. The $^{206}Pb/^{238}U$ dates of specimens without clusters range from 1450 ± 187 Ma to 1684 ± 200 Ma (Fig. 9a, Supplementary Table 3.

Out of five specimens analysed from the twin domain, two ran successfully (V7, V9), and showed two different types of clusters (Supplementary Fig. 2). Specimen V9 is characterised by Pb*-only clusters, with Pb* concentration up to 2.5 at. % (compared to 0.05 at. % in the matrix). In contrast specimen V7 shows Ca-rich clusters but with no Pb. The $^{207}Pb/^{206}Pb$ dates obtained are 1967 ± 2769 Ma (V7), and 2333 ± 975 Ma (V9, including Pb clusters). The $^{207}Pb/^{206}Pb$ matrix age of specimen V9 is 2186 ± 1092 Ma (Fig. 9a). Whole specimen $^{206}Pb/^{238}U$ dates (matrix + clusters) for V7 and V9 are 1319 ± 322 Ma and 1688 ± 223 Ma, respectively (Supplementary Table 3).

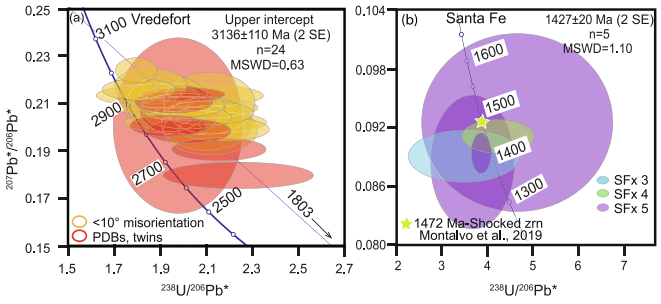

Fig. 6. SHRIMP U-Pb geochronology results plotted on Tera-Wasserburg diagrams. (a) Results for Vredefort xenotime grain 14DG14. Red ellipses – spots targeting twins and planar deformation bands; yellow ellipses – spots targeting areas with < 10° misorientation. The lower intercept of the discordia is 1803 ± 270 Ma. (b) Results for Santa Fe xenotime grains. The five analyses overlap and yield a concordia age of 1427 ± 20 Ma.

4.3.2. *Santa Fe xenotime (grain SFx5)*

Four of six APT specimens were analysed from xenotime SFx5. Specimen SF1 is from the host, SF2 targeted a host-twin boundary, and specimens SF3 and SF4 are from the same {1 1 2} lamellar twin (Fig. 3h). SF1 and SF2 are characterised by the presence of numerous small (~5 to 20 μm) Ca-Pb* enriched clusters (Fig. 8b). The Ca concentration is up to 3.6 at. % in clusters, as compared from 0.07 at. % in the matrix; Pb concentration also increases up to 1 at. % from 0.08 at. %. In addition to the small Ca-Pb* clusters, specimen SF3 is characterised by one large (~18 nm) cluster in which the Pb* enrichment is higher (from 0.08 to ~6 at. % Pb), with Ca (0.07 to 2.5 at. %) and Si (0.08 to 1.6 at. %). In specimen SF4, there are numerous Ca-rich clusters with no Pb, and one cluster with Pb* enrichment from 0.08 to ~3.8 at. %, and Si (0.08 to 1.8 at. %) (Fig. 8b). The $^{206}Pb/^{238}U$ dates do not show significant variation between host and twin domains. The $^{206}Pb/^{238}U$ dates obtained are 1275 ± 69 Ma, 1319 ± 45 Ma, 1391 ± 83 Ma, 1274 ± 100 Ma (2σ) from SF1, SF2, SF3 and SF4 respectively with a weighted mean date of 1316 ± 69 Ma (2σ, MSWD = 1.8, p = 0.14) (Fig. 9b). The matrix ages from specimens SF3 and SF4 yield a $^{206}Pb/^{238}U$ date of 1329 ± 81 Ma and 1213 ± 98 Ma, respectively, which is within uncertainty of the whole specimen date (Supplementary Table 3).

4.3.3. *Araguainha xenotime (grain X3)*

Five specimens were prepared from grain X3, and three successfully analysed by APT. One specimen targeted the grain boundary between two neoblasts (A4), one specimen sampled a ~3 μm neoblast with no internal misorientation (grain α) and the other a ~1 μm neoblast (grain β) with internal misorientation up to ~7°. In orientation maps, grain α

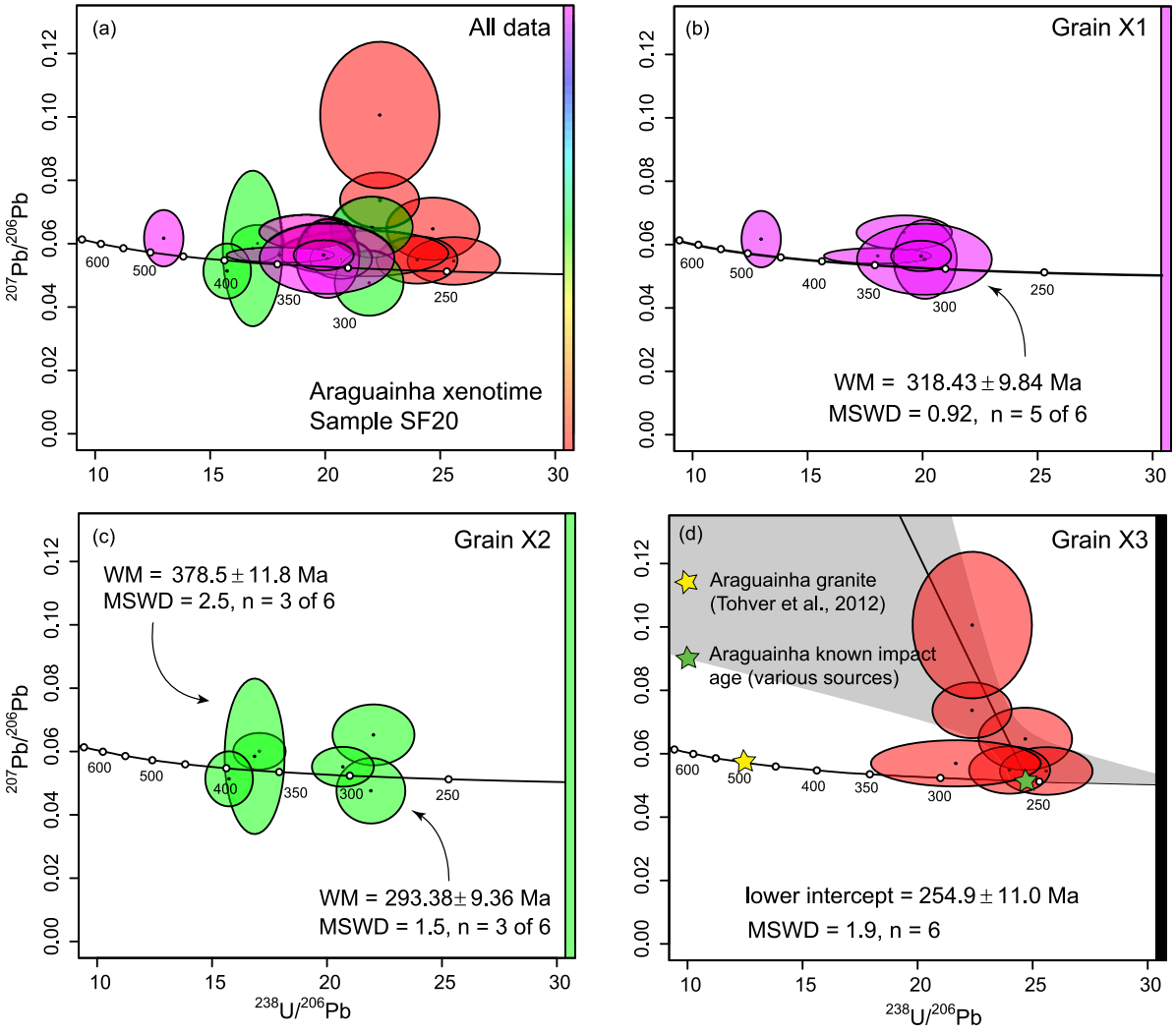

Fig. 7. SHRIMP U-Pb results plotted on Tera-Wasserburg diagram from grains from Araguainha. (a) Complied results from grains X1, X2 and X3. (b) Results from grain X1 showing one main age cluster. (c) Results from X2, showing two main age clusters. (c) Results from X3; all six analyses yield a lower concordia intercept of 254.9 ± 11 Ma.

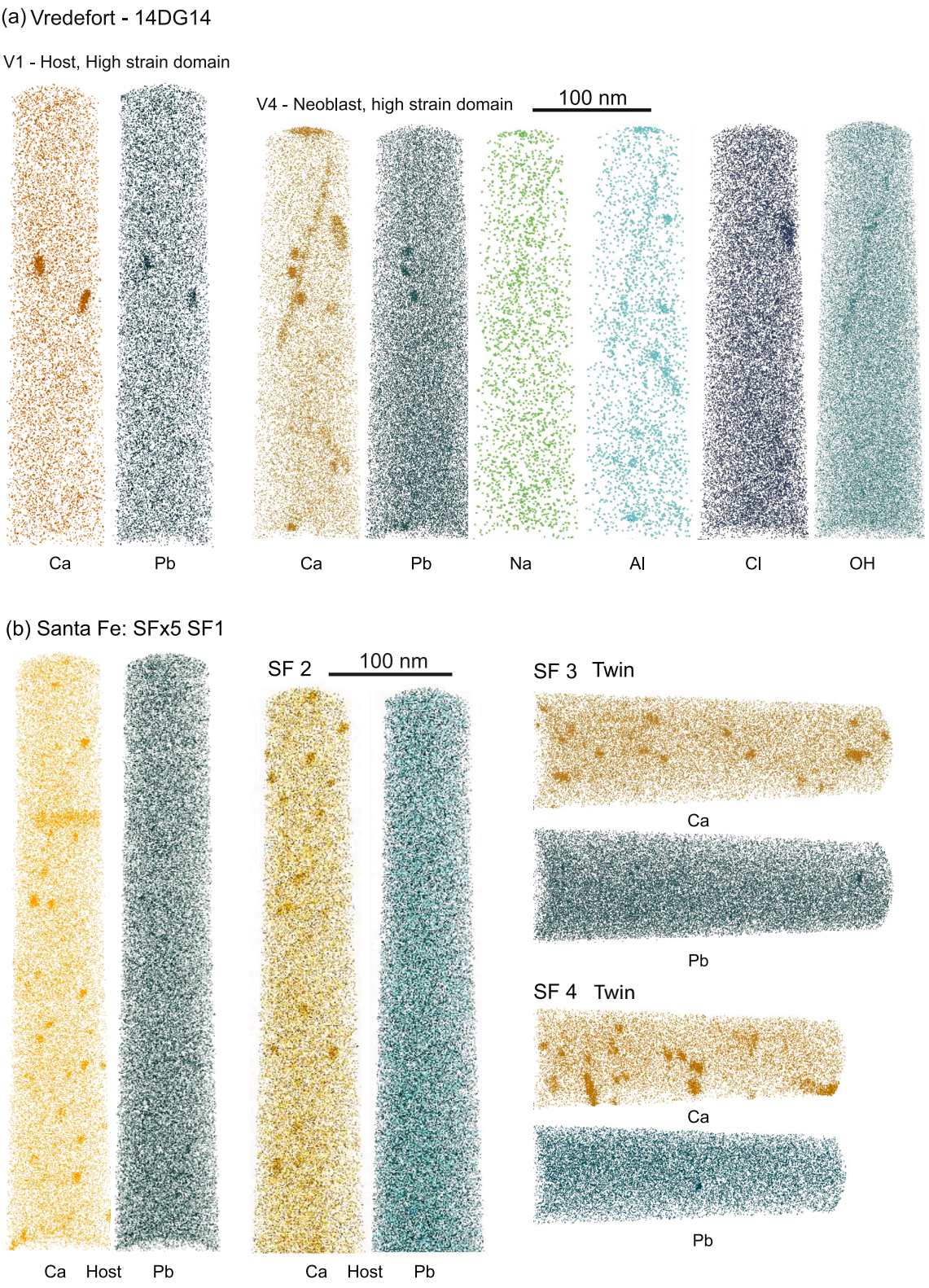

Fig. 8. Atom probe 3D reconstruction of representative specimens from Vredefort xenotime grain 14DG14 and Santa Fe grain SFx5. Each small sphere represents an atom of the indicated element. (a) Vredefort specimen V1, host xenotime from a high strain domain showing Ca and Pb* enriched clusters and a dislocation enriched in Ca, Na, Al, and OH. Cl is also distributed heterogeneously in clusters. Specimen V4 is from a neoblast and shows Ca and Pb* enriched clusters. (b) Santa Fe specimens SF1 and SF2 from host, and SF3 and SF4 from twin domains. Host and specimen show numerous Ca clusters with < 1 % Pb* clusters. Note that Pb* enriched Ca clusters are only present in specimens from the twin domain.

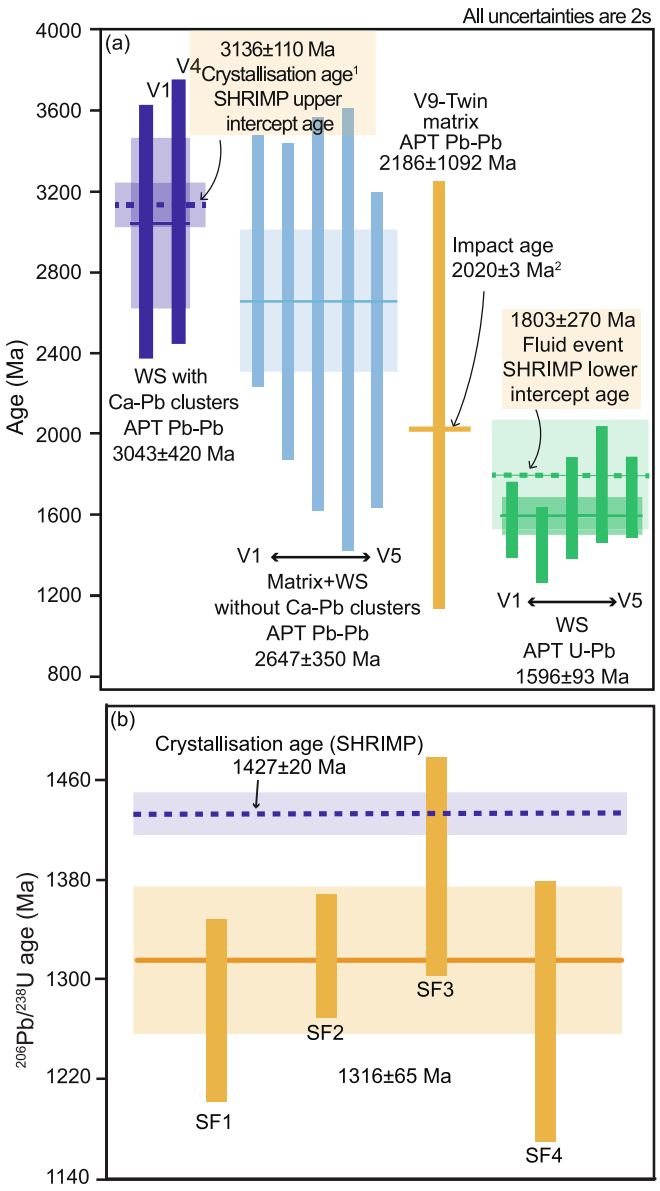

Fig. 9. (a) Summary of both Pb-Pb and U-Pb APT nanogeochronology results obtained from the different domains (neoblastic and twin) for Vredefort grain 14DG14 ([1]Hart et al., 1981; [2]Kamo et al., 1996) (WS – Whole atom probe specimen). (b) U-Pb nanogeochronology results from the four specimens from Santa Fe grain SFx5.

protrudes into grain β, producing a lobate grain boundary (Fig. 4g); this grain boundary was captured in APT specimen A4. The geometrical orientation of APT specimen A4 relative to the polished surface of the grain was monitored during FIB sample preparation and loading/analysis by APT. The boundary is conspicuously enriched in a range of elements compared to the matrix, including Si = 2.67 (vs. 0.10) at. %, Mg = 1.21 (vs. 0.06) at. %, Ca = 1.01 (vs. 0.15) at. %, Cl = 0.72 (vs. 0.13) at. %, Na = 0.23 (vs. 0.01) at. %, and Al = 0.26 (vs. 0.01) at. % (Fig. 10). In A4 numerous Si- and Mg-rich clusters (Si up to 7.5 at. %, Mg up to 1.5 at. %) 5 to 20 nm in diameter are present in grain β (small and minor internal misorientation) whereas only a few Si-Mg clusters are present in grain α (large and no misorientation). Other APT specimens analysed (A2, A5) contain dislocations enriched in Ca, Si, Mg, Na, and Al. No Pb isotopes were detected above background, therefore no age data are available from any of the Araguainha xenotime APT specimens.

Fig. 10. Specimen A4 from Araguainha showing grain boundary enriched in elements such as Si, Mg, Ca, Cl, Na, Al. The specimen also shows the presence of Si-Mg clusters with variable distribution in different grains.

5. Discussion

5.1. Shock microstructures in xenotime

The xenotime grains investigated in this study originate from different sites and different crater environments (where known). The grains show a variety of crystal-plastic deformation microstructures that were investigated to evaluate the response of the U-Pb system. Microstructures investigated include PF, PDB, deformation twin lamellae, as well as grains that have partially or fully recrystallised to neoblastic (granular) domains. The following section summarises the microstructures in the grains studied in the context of previous descriptions of shocked xenotime.

5.1.1. Planar fractures (PF)

Planar fractures have been documented in xenotime grains from the Santa Fe (Fig. 3; Cavosie et al., 2016a) and Spider (Cox et al., 2021) impact structures, and here we report an example of PF in xenotime from the Vredefort impact structure. Four orientations of PF were documented in Vredefort xenotime 14DG14 (Fig. 2). In all cases thus far described, PF consist of multiple sets of closely spaced (1 to 5 μm) penetrative parallel fractures that typically extend fully across grains (or nearly so). In two of the three Santa Fe grains analysed (grains SFx2, SFx4), as well as the Vredefort grain (14DG14), one or more sets of PF were found to contain {1 1 2} deformation twins (Fig. 3). However, twins were not identified in Santa Fe grain SFx3, and twins were also not present in several PF-bearing xenotime grains documented by Cox et al. (2021). This observation demonstrates that deformation twins can not be assumed to be present in xenotime grains that contain PF. In this regard, PF in xenotime appear analogous to those in zircon; they seem to be a common microstructure in shocked grains, but alone they do not provide diagnostic evidence of shock deformation.

5.1.2. Planar deformation bands (PDB)

The presence of PDB have been documented in xenotime grains from the Vredefort (Cavosie et al., 2021), Santa Fe (Cavosie et al., 2016a), and Spider (Cox et al., 2021) impact structures. The PDB described by Cavosie et al. (2021) in a Vredefort detrital xenotime occur in three discrete orientations, with individual PDB typically 5 to 10 μm wide, and preserving up to 40° of misorientation relative to the host grain. Significant misorientation across discrete 2–3 um-wide PDB were also described in xenotime grains from shatter cones in quartzite (Cox et al., 2021). The PDB in Vredefort xenotime 14DG14 described here mostly occur in areas bound by cross-cutting PF sets and near grain margins. They are generally 10–20 μm wide and are sub-parallel to PF sets, but some are irregular in shape and have diffuse boundaries with up to ~12° of misorientation relative to the host grain (Fig. 2c). The only significant PDB found in the Santa Fe xenotime grains occur in grain SFx5, and are concentrated near the margin of the grain (some are sub-parallel to PF set 3), and preserve up to 6° of misorientation from the host (Fig. 3c,f). The above observations highlight the magnitude of variable misorientations across PDB in xenotime grains from different impact structures. Similar to PF, PDB are not regarded as representing diagnostic evidence of shock deformation in xenotime, as is the case for both zircon (Timms et al., 2017) and apatite (Cox et al., 2020).

5.1.3. Deformation twins in {1 1 2}

Lamellar deformation twins are commonly found in shocked zircon (see discussion in Cavosie and Folco, 2021a), shocked monazite (Erickson et al., 2016), and shocked titanite (Timms et al., 2019). Deformation twins in shocked xenotime have thus far been reported in grains from the Vredefort, Santa Fe, and Spider impact structures (Cavosie et al., 2021; Cavosie et al., 2016a; Cox et al., 2021). Here we document {1 1 2} twins in Vredefort grain 14DG14 and also in Santa Fe grains SFx4 and SFx5 (the latter two were described previously). Lamellar deformation twins in {1 1 2} in xenotime are defined by a 65° misorientation from the ⟨1 1 0⟩ of the host grain and a shared {1 1 2} direction (Cavosie et al., 2016a, 2021; Cox et al., 2021). Formation conditions of {1 1 2} twins in xenotime have not been calibrated experimentally, however, empirical constraints suggest formation conditions of 5 to 20 GPa based on their occurrence in samples that contain shocked quartz and shocked zircon, as well as their presence in shatter cones (Cavosie et al., 2016a; Montalvo et al., 2019; Cox et al., 2021). A new observation of twin phenomenon here is the discontinuous nature of individual {1 1 2} twin lamellae in Vredefort xenotime 14DG14. In that grain, the t3 {1 1 2} twin preserves twin segments with different disorientations along the length of a single lamellae, including (72°/⟨3 4 2⟩, 68°/⟨2 3 2⟩, 70°/⟨3 4 1⟩, and 70°/⟨3 4 0⟩) (Fig. 2e). The segmented lamella could represent a progressive shear transformation to accommodate the geometry of {1 1 2} twins, or alternatively, the lamellar twin may have responded in a heterogeneous way to localised stresses that effectively fractured the lamella during twin formation, resulting in multiple orientations of 'failed twin' domains along its length. Alternatively post-impact partial annealing could also have modified the lamellar twin, as has been discussed for zircon (Erickson et al., 2013b).

5.1.4. Recrystallisation to neoblastic texture

There are few reports of neoblastic (granular) textures in xenotime from shocked rocks. Multiple examples of polycrystalline xenotime grains consisting of aggregates of low strain ~1 μm sized neoblasts were reported from the Spider impact structure by Cox et al. (2021), occurring in shatter cone samples of quartzite that contained quartz with PDF and shock-twinned zircon. However, in most cases the polycrystalline xenotime grains occurred in cracks and vugs; it was therefore not clear if the polycrystalline microstructures formed by impact processes, or if they had a diagenetic/secondary origin, as systematic orientation relations among the neoblasts were not observed. Only one xenotime grain described by Cox et al. that consisted of both recrystallised polygonal neoblasts and a strained host domain with PDB had an unambiguous impact origin. In this study neoblastic microstructures were found in Vredefort grain 14DG14 and in all three Araguainha xenotime grains.

Vredefort grain 14DG14 contains rare localised occurrences of 2–3 μm sized neoblasts along PF planes that also contain {1 1 2} twins (Fig. 2d). The neoblasts are generally round and isolated in occurrence and are a very minor microstructural feature of grain 14DG14. Given their location on PF planes that elsewhere contain {1 1 2} twins, the origin of these neoblasts is likely related to local shear-stress induced recrystallisation that was energetically insufficient to form a lamellar twin. The stored strain energy lowered the energy barrier for nucleation, forming neoblasts locally via grain boundary migration (Erickson et al., 2017). Given their rarity in grain 14DG14, it is unlikely that the neoblasts in this grain formed via thermal recrystallisation process (Moser et al., 2011; Erickson et al., 2017).

In contrast, EBSD analysis shows that the three Araguainha xenotime grains from impact melt rock sample SF20 reported here contain variable amounts of recrystallised neoblastic domains. Grain X1 consists mostly of a strained host domain (~86 %) that preserves up to 20° of accumulated misorientation across the grain. The strained host domain does not contain other discrete microstructures, such as PDB or deformation twins. Two populations of neoblasts comprise 14 % of grain X1; each shares a systematic orientation with the host domain of 65°/⟨1 1 0⟩ and a shared {1 1 2} direction (Fig. 5). Both populations of neoblasts are thus interpreted to have formed by the recrystallisation of former {1 1 2} deformation twins, similar to that reported in some granular zircon grains (Cavosie et al., 2016b), and also in partially recrystallised monazite (Erickson et al., 2015). Xenotime grains X2 and X3 consist entirely of recrystallised neoblasts, however, no systematic orientation relations indicative of recrystallised twins are present in either grain (Fig. 4). In grain X2, the majority of neoblasts are dispersed about the c-axis (Fig. 4b). Grain X3 contains a central area approximately 40 μm × 20 μm that consists of neoblasts that preserve the host grain orientation; neoblasts in different orientations form a wide margin around the central area (Fig. 4d,f). In general, neoblasts in all Araguainha xenotime grains preserve high angle boundaries (>10°) with adjacent neoblasts. The host rock of the Araguainha xenotime grains is an impact melt rock derived from a sedimentary rock, and likely become molten during shock pressures >20 GPa and subsequent heating (Stöffler et al., 2018).

5.2. SIMS U-Pb geochronology of shock microstructures in xenotime

5.2.1. Shock twins, PDB, and PF in xenotime (Vredefort & Santa Fe)

A total of 24 SHRIMP spot analyses made on Vredefort grain 14DG14 yield a discordant array with an upper concordia intercept of c. 3136 Ma which is interpreted as the crystallisation age of the grain, as it broadly overlaps ages of basement gneisses exposed at the Vredefort impact structure (3.5 to 3.1 Ga, Hart et al., 1981; Flowers et al., 2003; Moser et al., 2011). The SHRIMP analyses overlapped {1 1 2} twins, PDB, and PF, however no correlations between age and microstructure were detected. At the scale of the SIMS analysis, the shock microstructures targeted here do not record Pb-loss related to the impact event, similar to a previous report for a different shocked xenotime grain from the Vredefort structure (Cavosie et al., 2021).

The five SIMS analyses of three Santa Fe xenotime grains include spots on {1 1 2} twins, PDB, and PF. The five analyses are concordant and yield a weighted mean $^{207}Pb^*/^{206}Pb^*$ age of 1427 ± 20 Ma. The age of the Santa Fe impact event is not well constrained (see Fackelman et al., 2008; Montalvo et al., 2019), and the granites in the area have not previously been dated. However, the Mesoproterozoic age determined here is best interpreted as the crystallisation age of the host granitoid. Detrital zircon grains throughout the area where shatter cones are exposed mostly range in age from 1.7 to 1.4 Ga, and the 1427 ± 20 Ma age determined here overlaps with the 1472 ± 35 Ma age determined from detrital shocked zircon in the same area (Montalvo et al., 2019).

In summary, no apparent impact age resetting associated with PF,

PDB, and deformation twins in xenotime was detected at the scale of SIMS analyses from the Vredefort and Santa Fe impact structures. In this regard, the U-Pb response of these shock microstructures in xenotime are thus similar to those in zircon (Moser et al., 2011; Erickson et al., 2013a; Cavosie et al., 2015, 2018a; Montalvo et al., 2019; McGregor et al., 2019).

5.2.2. Neoblast formation in Araguainha – Pb mobility and age resetting

The three xenotime grains from Araguainha were each analysed in six locations by SIMS. Analysis spots on grain X1 were mostly mixtures of host and neoblasts, whereas all analyses on grain X2 were on neoblasts. Grains X1 and X2 both show coherent clusters on concordia diagrams, however, none of the age clusters coincides with the known impact age. All spot analyses on grain X3 were on neoblasts, and common Pb was also detected. Grain X3 is the only grain to yield a reset age that coincides with the known impact age (255 ± 11 Ma, MSWD = 1.9, n = 6). The oldest spot analysis measured on any of the Araguainha xenotime grains is 478 ± 25 Ma (grain X1, host domain). This age overlaps with the crystallisation age of the Araguainha granite (512 ± 11 Ma, Tohver et al., 2012), suggesting that the xenotime grains analysed from sample SF20 are likely to have been sourced from the Araguainha granite. The SHRIMP U-Pb results indicate that solid-state recrystallisation of xenotime in impact melt rocks leads to the formation of neoblasts with variable U-Pb resetting. The spread of data between the inferred crystallisation age and the impact age represents variable Pb-loss, and such ages likely have no geological significance. The neoblastic (granular) texture in xenotime is thus the prime candidate microstructure to target for dating impact events, as has been observed in other minerals such as zircon and monazite (Moser et al., 2011; Cavosie et al., 2015; Erickson et al., 2017; Kenny et al., 2017; Erickson et al., 2020; McGregor et al., 2019).

5.2.3. Significance of the Vredefort xenotime lower discordia intercept

The SIMS data for Vredefort xenotime 14DG14 define a discordia line with an imprecise lower concordia intercept of 1803 ± 270 Ma. Due to the high uncertainty, this age overlaps with both the c. 2020 Ma impact age and a lower concordia intercept age of 1754 ± 150 Ma previously determined on detrital shocked xenotime grain from the Vredefort impact structure (Cavosie et al., 2021). The 1754 ± 150 Ma age was interpreted to record a unknown alteration event in the Witwatersrand basin (Cavosie et al., 2021). An age of 1772 ± 150 Ma from a Vredefort shocked monazite grain was determined in an APT study and interpreted to represent an alteration event that formed nanoscale element clusters in monazite (Fougerouse et al., 2021a). To date, Paleoproterozoic ages (1.8–1.7 Ga) in shocked minerals from the Vredefort impact structure have only been reported in monazite (Flowers et al., 2003; Fougerouse et al., 2021a) and xenotime (this study; Cavosie et al., 2021); they have conspicuously not been reported in U-Pb studies of Vredefort shocked zircon (e.g., Flowers et al., 2003; Armstrong et al., 2006; Moser et al., 2011).

Post-impact age resetting has been reported in other shocked minerals from other impact structures. Shocked baddeleyite from Sudbury impact melt sheet was shown to record post-impact metamorphic signatures (White et al., 2017). The formation of shock deformation microstructures such as planar fractures and deformation twins may enhance the mobility of elements through fast diffusion pathways. The new pathways formed due to shock deformation may render the mineral susceptible to younger (post-impact) Pb loss events, especially for phases more readily susceptible to fluid alteration, such as phosphates. The above results further demonstrate that impact metamorphism enhances the susceptibility of certain minerals to post-impact metamorphic or hydrothermal events.

5.3. Nanoscale heterogeneities in shock-deformed xenotime

5.3.1. Nanoscale analysis of twins and neoblasts from Vredefort and Santa Fe

The APT specimens from areas of high lattice misorientation in the Vredefort xenotime (Fig. 2d) are characterised by the presence of small, strain-free neoblasts that contain Ca-Pb* rich clusters in two out of five specimens analysed. The largest cluster from specimen V4 (Fig. 8a) is composed of 7.2 at. % Ca, 2.67 at. % Pb, and 0.8 at. % Si, with a combined Ca + Pb + Si concentration of 10.67 at. %. Such a composition suggests that the cluster is likely a nanoscale inclusion of a different phase (Fougerouse et al., 2016, 2018, 2021a; Seydoux-Guillaume et al., 2019), rather than a trace element enriched domain of xenotime, as has been observed in zircon and rutile (Valley et al., 2014; Peterman et al., 2016, 2019; Verberne et al., 2020). The chemical composition of the clusters is most consistent with the mineral apatite $Ca_5(PO_4)_3(OH,F,Cl)$, in which Pb can substitute for Ca (Pan and Fleet, 2002). The $^{207}Pb/^{206}Pb$ APT age obtained from the two specimens with Ca-Pb* clusters are 3043 ± 420 Ma, which is consistent with the inferred crystallisation age of the sample (Fig. 9a). Excluding the clusters, combining the matrix of the same specimens and the specimens devoid of the Ca-Pb* clusters yields a weighted mean $^{207}Pb/^{206}Pb$ age of 2647 ± 350 Ma. On the assumption that all Pb* migrated into the clusters during formation, the $^{207}Pb/^{206}Pb$ 2647 ± 350 Ma matrix age represents the age of cluster formation (Fig. 9a). One specimen (V4) from the high strain domain contains OH-enriched clusters, and a linear feature enriched in Na, Al, and Cl which is interpreted as a dislocation based on previous APT studies (Piazolo et al., 2016; Fougerouse et al., 2021a; Verberne et al., 2022). Specimen V5 presents a set of dislocations in a planar domain which is enriched in elements such as Si, Ca, Cl, Na, and Al (Supplementary Fig. 2). The geometry is consistent with that of low angle boundaries in olivine (Tacchetto et al., 2021). All ions present in the dislocations are not part of the mineral xenotime and instead record nanoscale evidence of fluid activity in the sample (Tacchetto et al., 2021; Joseph et al., 2023). Therefore, we suggest that the apatite inclusions formed during a post-crystallisation fluid alteration event at 2647 ± 350 Ma. The date of 2647 ± 350 Ma also overlaps with ~2729–2665 Ma Ventersdorp volcanism in South Africa (Schneiderhan et al., 2011; Altermann and Lenhardt, 2012; Gumsley et al., 2020). However, the high uncertainty associated with the APT dates precludes a robust determination of causation (V1-V5, Fig. 9a). Whole sample (matrix + clusters) APT $^{206}Pb/^{238}U$ dates from these five specimens yield a weighted mean age of 1596 ± 93 Ma. The younger $^{206}Pb/^{238}U$ age obtained from whole specimen data overlaps with the cryptic post-impact alteration event reported previously in both xenotime and monazite (Cavosie et al., 2021; Fougerouse et al., 2021a). Two APT specimens analysed from {1 1 2} twin domains (Fig. 2e) also show a different type of cluster, one with enrichment of only Ca and one with enrichment of only Pb. The $^{207}Pb/^{206}Pb$ date obtained from the matrix of the specimen with Pb* clusters is 2186 ± 1092 Ma, which broadly coincides with the known impact age of ~2020 Ma, however no conclusion can be made with the low precision data (Fig. 9a).

In the case of Santa Fe xenotime SFx5, nanoscale analysis of the xenotime host and {1 1 2} twin reveals nanoscale Ca-enriched clusters (up to 4 at. % Ca) with varying Pb* concentration (between 1 and 3.8 at. % Pb) between specimens (Fig. 8b). The low Pb* containing clusters are only seen in specimens from the host (SF1 and SF2), and not from the twin domain (SF3 and SF4). The absence or low concentration (maximum of ~1 at. %) of Pb* in the small Ca-enriched clusters suggests the clusters formed in a short time span after crystallisation. The mechanism behind cluster formation in the absence of fluids is presumably the exsolution of apparently bigger Ca^{2+} (1.12 Å) and Pb^{2+} (1.29 Å) ions compared to the Y^{3+} (1.02 Å) ion, due to the size disparity during cooling of the crystal (Shannon, 1976). This phase immiscibility model has been proposed to form nanoscale apatite inclusions in previous xenotime and monazite atom probe studies (Fougerouse et al., 2018; Joseph et al., 2021).

The APT specimens SF3 and SF4 from the twin domain of the Santa Fe grain contain Ca clusters with higher Pb* enrichment, up to 6 at. % (SF3) compared to other Ca-Pb clusters from the Santa Fe gain, in which the Pb* concentration is less than 1 at. %. The higher Pb* concentration in these clusters indicates formation a considerable period of time after crystallisation. Nanoscale mobility of Pb into clusters during twin formation has been documented during crystal plastic deformation of monazite, both in tectonic and shock settings with apparent temperature control (Fougerouse et al., 2021a, b). It is thus possible that the Pb*-rich clusters formed at the time of twin formation during shock deformation. However, the $^{206}Pb/^{238}U$ nanogeochronology dates of SF3 and SF4 from the whole specimen (SF3 – 1391 ± 83 Ma, SF4 – 1274 ± 100 Ma) overlap with the respective dates obtained from the matrix (SF3 – 1329 ± 81 Ma, SF4 – 1213 ± 98 Ma), and it is therefore not possible to confirm if they formed during twinning. Considering the data for xenotime samples from Vredefort and Santa Fe, there is an indication of Pb mobility associated with twin formation, however it is not conclusive due to low the precision of available data.

5.3.2. *Nanoscale analysis of neoblasts from Araguainha*

In Araguainha xenotime samples, the Pb signal in the atom probe mass spectra was not significantly above background, and therefore no APT nanogeochronology data could be extracted for these samples. The grain boundary analysed between two neoblasts and the dislocations from Araguainha grain X3 (specimen A4) are enriched primarily with Si, followed by Mg, Ca, Cl, Na and Al. In addition, Si-Mg clusters are distributed preferably on one side of the grain boundary in specimen A4. Elements such as Si and Ca can be incorporated into xenotime by cheralite and huttonite substitution (Spear and Pyle, 2002). The rest of the elements found along the grain boundary (Cl, Na and Al) are not commonly present in xenotime, and could have been derived from an external source, such as fluids (e.g., Tacchetto et al., 2021, 2022).

Trace element migration is found to be intimately associated with the defect density in materials (Watanabe, 1985). The segregation of trace elements which are not inherently part of the host mineral to the grain boundary is more energetically favourable to reduce the lattice stress principally caused by the differences in ionic size between the host grain sites and the trace element (Hoskin and Black, 2000; Reddy et al., 2016). The enrichment of trace elements in dislocations and both low and high-angle boundaries has been documented in minerals from different geological settings (Suzuki, 1987; Hiraga et al., 2003; Reddy et al., 2016; Dubosq et al., 2018; Fougerouse et al., 2019; Tacchetto et al., 2021, 2022). Shock deformation produces high strain in minerals, resulting in numerous dislocations and low-angle boundaries. During annealing facilitated by high temperatures from melting of surrounding rocks, neoblasts nucleate from sub-grain boundaries through grain boundary migration (Doherty et al., 1997; Piazolo et al., 2012). Grain boundary migration occurs when a grain with low degrees of imperfection grows into a grain with higher degree of dislocations and low angle boundaries creating a lobate inter-fingering texture (Poirier, 1985; Jessell, 1987; Passchier and Trouw, 2005; Drury and Pennock, 2007). This texture can be seen in the neoblasts selected for nanoscale APT analysis, where a grain with no internal misorientation is seen growing into a grain with higher internal misorientation along a lobate texture (Fig. 4h).

The difference in the degree of internal misorientation in a neoblast is reflected in the composition from APT analysis, which shows a difference in the density of Si-Mg clusters from one neoblast to another. The orientation of the boundary in the APT specimen coincides with the orientation of the boundary determined by EBSD (Figs. 4 and 10). In the APT specimen, the domain above the grain boundary corresponds to the neoblast with no misorientation identified from EBSD (Fig. 4h) and has a limited number of nanoscale Si-Mg clusters (Fig. 10). The domain below the grain boundary in the APT specimen corresponds to the neoblast with higher degree of internal misorientation and is characterised by a higher density of nanoscale Si-Mg clusters (Fig. 10). These observations suggest that the grain boundary of the neoblasts with no misorientation (grain α, Fig. 11) displaced Si-Mg clusters during its migration, forming strain-free neoblasts during the recovery stage of shock deformation, forming the lobate texture (Passchier and Trouw, 2005; Fig. 11). The formation of defects, grain boundaries and neoblasts is very rapid as inherent to impact metamorphism; further growth of neoblasts can continue if sufficient temperature is provided. The process of grain boundary migration reduces strain in a crystal, and it is here hypothesised that Pb* was collected by the grain boundaries and diffused to the grain edges. Pb is a large cation in the xenotime structure (Cherniak, 2006), and it is likely to diffuse out of the crystal lattice during grain boundary migration through high-diffusivity pathways and dislocation pipe diffusion (Love, 1964). This process would result in resetting the U-Pb age recorded in the grain. The higher amount of recrystallisation through this process would result in a higher degree of Pb loss from the grain, as observed from the grains from X1 to X3.

Alternatively, the trace element enrichment in the grain boundary

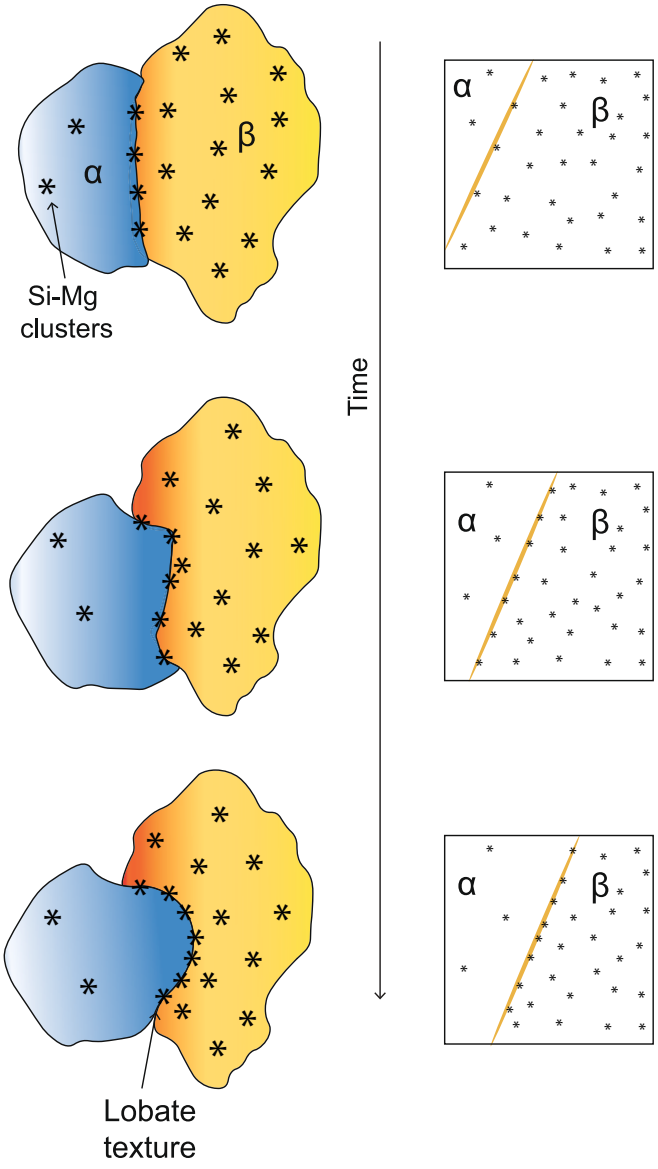

Fig. 11. Illustration of grain boundary migration forming a lobate texture between the recrystallised neoblasts at the grain scale (left) and nanoscale (right). Crystal α has a lower dislocation density, a smaller number of clusters hence less crystal distortion. Crystal β has a higher cluster density, with internal misorientation. With time, more deformed crystal is consumed, by atoms from crystal β reorganising to fit the crystal lattice of crystal α, forming a interfingering lobate texture.

may represent a melt phase. In granular neoblastic zircon void spaces between neoblasts can contain melt glass, lechatelierite, or other minerals (Moser et al., 2011; Cavosie et al., 2016b, 2018b,c). In the Araguainha xenotime, the composition of Si reaches ~2.6 at. %, which is likely not high enough to represent a silicate impact melt composition (~70 wt% SiO_2 in melt veins from Araguainha melt veins, Machado et al., 2009).

6. Conclusions

Here we evaluated the ability of xenotime to date meteorite impact events. Shock microstructures observed in xenotime from three known impact structures Vredefort, Santa Fe and Araguainha include PF, PDB, varying degrees of lattice misorientation, shock deformation {1 1 2} twins, and the newly identified shock-induced polycrystalline neoblastic texture. Whilst {1 1 2} twins and PDB show no apparent impact related resetting, neoblastic (granular) textured xenotime shows an apparent correlation between the extent of recrystallisation and the degree of U-Pb age resetting. In the most extreme case, fully recrystallised neoblastic xenotime yields the age of the Araguainha impact event (255 ± 11 Ma). At nanoscale, the neoblasts show elemental clusters that chemically resemble apatite, dislocations, and grain boundaries with higher concentration of trace elements such as Si, Mg, Ca, Na, Cl, and Al. The asymmetrical distribution of clusters across a grain boundary between two neoblasts suggests their formation through grain boundary migration process. The shock origin of neoblastic textures in xenotime can be used to constrain ages of impact events when grains are fully recrystallised, but we caution that partially neoblastic xenotime may yield apparent dates that are partway between the pre-impact crystallisation age and the impact event.

Data availability

Data are available through Mendeley Data at https://data.mendeley.com/datasets/4w7x79vtk2/1.

CRediT authorship contribution statement

Cilva Joseph: Writing – review & editing, Writing – original draft, Visualization, Project administration, Investigation, Formal analysis, Data curation, Conceptualization. **Denis Fougerouse:** Writing – review & editing, Visualization, Validation, Supervision, Project administration, Funding acquisition, Formal analysis, Data curation, Conceptualization. **Aaron J. Cavosie:** Writing – review & editing, Visualization, Validation, Software, Resources, Investigation, Formal analysis, Data curation, Conceptualization. **Hugo K.H. Olierook:** Writing – review & editing, Visualization, Validation, Software, Formal analysis, Data curation. **Steven M. Reddy:** Writing – review & editing, Supervision, Funding acquisition. **Tommaso Tacchetto:** Writing – review & editing, Visualization, Software, Data curation. **Raiza R. Quintero:** Writing – review & editing, Visualization, Formal analysis. **Allen Kennedy:** Writing – review & editing, Validation, Formal analysis, Data curation. **David W. Saxey:** Writing – review & editing, Validation, Supervision, Methodology, Formal analysis. **William D.A. Rickard:** Writing – review & editing, Data curation.

Declaration of competing interest

The authors declare that they have no known competing financial interests or personal relationships that could have appeared to influence the work reported in this paper.

Acknowledgements

Araguainha sample SF20 was provided by N. Hauser. Sample mount 05-12 used for xenotime standard in this project is part of the McNaughton Legacy Collection, in the John de Laeter Centre (JdLC). This study benefited from the Australian Science and Industry Endowment Fund (grant SIEF RI13-01) and the Discovery Early Career Research Award from the Australian Research Council to Denis Fougerouse (DE190101307). The authors acknowledge the support of Microscopy and Microscopy Facility and JdLC, Curtin University, whose instrumentation has been supported by University, State and Commonwealth Government funding. Tsuyoshi Iizuka and Jeffrey G. Catalano are thanked for editorial handling, and two anonymous reviewers are thanked for providing constructive comments.

Appendix A. Supplementary material

Supplementary materials provide (i) Supplementary Table 1: EBSD working conditions, (ii) Supplementary Table 2: EPMA composition results from the samples, (iii) Supplementary Table 3: APT nanogeochronology data from Vredefort and Santa Fe samples (iv) Supplementary Fig. 1: EBSD GROD angle map of grain X3 from Araguainha, and (v) Supplementary Fig. 2: 3d reconstruction profiles of APT specimens analysed from Vredefort and Araguainha which is not shown in the main draft. Supplementary material to this article can be found online at https://doi.org/10.1016/j.gca.2024.04.017.

References

Aleinikoff, J.N., Hayes, T.S., Evans, K.V., Mazdab, F.K., Pillers, R.M., Fanning, C.M., 2012. SHRIMP U-Pb ages of Xenotime and monazite from the Spar Lake red bed-associated Cu-Ag deposit, western Montana: Implications for ore genesis. Econ. Geol. 107, 1251–1274.

Altermann, W., Lenhardt, N., 2012. The volcano-sedimentary succession of the Archean Sodium Group, Ventersdorp Supergroup, South Africa: Volcanology, sedimentology and geochemistry. Precambrian Res. 214–215, 60–81.

Armstrong, R.A., Lana, C., Uwe, R.W., Gibson, R.L., 2006. SHRIMP zircon age constraints on Mesoarchean crustal development in the Vredefort dome, central Kaapvaal Craton, South Africa. In Processes on the Early Earth (eds. W. U. Reimold and R. L. Gibson). Geol. Soc. Am. 405, 233–253.

Bauer, P.W., and Ralser, S., 1995, The Picuris-Pecos fault: Repeatedly reactivated, from Proterozoic to Neogene, in Bauer, P.W., Kues, B.S., Dunbar, N.W., Karlstrom, K.E., and Harrison, B., eds., Geology of the Santa Fe Region: Socorro, New Mexico, USA, New Mexico Geological Society 46th Annual Fall Field Conference Guidebook, 111–115.

Bauer, P., Ralser, S., Daniel, C., Ilg, B., and Harrison, B., 1996, Geologic map of the McClure Reservoir quadrangle, Santa Fe County, New Mexico: New Mexico Bureau of Geology and Mineral Resources, Open-File Geologic Map 07, scale 1:24,000, 1 sheet.

Bodorkos, S., Bowring, J.F., Rayner, N.M., 2020. Squid3: next-generation data processing software for sensitive high-resolution ion microprobe (SHRIMP). Geoscience Australia, Canberra.

Brown, S.M., Fletcher, I.R., Stein, H.J., Snee, L.W., Groves, D.I., 2002. Geochronological Constraints on Pre-, Syn-, and Postmineralization Events at the World-Class Cleo Gold Deposit, Eastern Goldfields Province, Western Australia. Econ. Geol. 97, 541–559.

Cavosie A. J. and Folco L. (2021a) Shock-twinned zircon in ejecta from the 45-m-diameter Kamil crater in southern Egypt eds. W. U. Reimold and C. Koeberl. Large Meteor. Impacts Planet. Evol. Geological Society of America Special Paper VI 550, 419–430.

Cavosie, A.J., Erickson, T.M., Timms, N.E., Reddy, S.M., Talavera, C., Montalvo, S.D., Pincus, M.R., Gibbon, R.J., Moser, D., 2015. A terrestrial perspective on using ex situ shocked zircons to date lunar impacts. Geology 43, 999–1002.

Cavosie A. J., Erickson T. M., Montalvo P. E., Prado D. C., Cintron N. O. and Gibbon R. J. (2018a) The Rietputs Formation in South Africa eds. Moser, D.E., Corfu, F., Darling, J.R., Reddy, S.M., and Tait K. Microstructural Geochronology: Planetary Records Down to Atom Scale, Geophysical Monograph American Geophysical Union. 232, 203–224.

Cavosie, A.J., Montalvo, P.E., Timms, N.E., Reddy, S.M., 2016a. Nanoscale deformation twinning in xenotime, a new shocked mineral, from the Santa Fe impact structure (New Mexico, USA). Geology 44, 803–806.

Cavosie, A.J., Timms, N.E., Erickson, T.M., Hagerty, J.J., Hörz, F., 2016b. Transformations to granular zircon revealed: Twinning, reidite, and ZrO2 in shocked zircon from Meteor Crater (Arizona, USA). Geology 44, 703–706.

Cavosie, A.J., Timms, N.E., Erickson, T.M., Koeberl, C., 2018b. New clues from Earth's most elusive impact crater: Evidence of reidite in Australasian tektites from Thailand. Geology 46, 203–206.

Cavosie, A.J., Timms, N.E., Ferrière, L., Rochette, P., 2018c. FRIGN zircon-The only terrestrial mineral diagnostic of high-pressure and high-temperature shock deformation. Geology 46, 891–894.

Cavosie, A.J., Kirkland, C.L., Reddy, S.M., Timms, N.E., Talavera, C., Pincus, M.R., 2021. Extreme plastic deformation and subsequent Pb loss in shocked xenotime from the

Vredefort Dome, South Africa. Large Meteorite Impacts and Planetary Evolution VI Geological Society of America VI 550, 465–478.
Cavosie, A.J., Spencer, C.J., Evans, N., Rankenburg, K., Thomas, R.J., Macey, P.H., 2022. Granular titanite from the Roter Kamm crater in Namibia: Product of regional metamorphism, not meteorite impact. Geosci. Front. 13, 101350.
Cherniak, D.J., 2006. Pb and rare earth element diffusion in xenotime. Lithos 88, 1–14.
Cherniak, D.J., 2010. Diffusion in accessory minerals: Zircon, titanite, apatite, monazite and xenotime. Rev. Mineral. Geochemistry 72, 827–869.
Chew, D.M., Petrus, J.A., Kamber, B.S., 2014. U-Pb LA–ICPMS dating using accessory mineral standards with variable common Pb. Chem. Geol. 363, 185–199.
Cox, M.A., Erickson, T.M., Schmieder, M., Christoffersen, R., Ross, D.K., Cavosie, A.J., Bland, P.A., Kring, D.A., Gulick, S., Morgan, J.V., Carter, G., Chenot, E., Christeson, G., Claeys, P., Cockell, C., Coolen, M.J.L., Ferrière, L., Gebhardt, C., Goto, K., Jones, H., Kring, D.A., Lofi, J., Lowery, C., Ocampo-Torres, R., Perez-Cruz, L., Pickersgill, A., Poelchau, M., Rae, A., Rasmussen, C., Rebolledo-Vieyra, M., Riller, U., Sato, H., Smit, J., Tikoo, S., Tomioka, N., Whalen, M., Wittmann, A., Urrutia-Fucugauchi, J., Xiao, L., Yamaguchi, K.E., 2020. High-resolution microstructural and compositional analyses of shock deformed apatite from the peak ring of the Chicxulub impact crater. Meteorit. Planet. Sci. 55, 1715–1733.
Cox, M.A., Cavosie, A.J., Poelchau, M., Kenkmann, T., Bland, P.A., Miljković, K., 2021. Shock deformation microstructures in xenotime from the Spider impact structure, Western Australia. In Large Meteorite Impacts and Planetary Evolution VI (eds. W. U. Reimold and C. Koeberl). Geol. Soc. Amer. Sp. Pap. 550, 449–464.
Darling, J.R., Moser, D.E., Barker, I.R., Tait, K.T., Chamberlain, K.R., Schmitt, A.K., Hyde, B.C., 2016. Variable microstructural response of baddeleyite to shock metamorphism in young basaltic shergottite NWA 5298 and improved U-Pb dating of Solar System events. Earth Planet. Sci. Lett. 444, 1–12.
Doherty, R.D., Hughes, D.A., Humphreys, F.J., Jonas, J.J., Jensen, D.J., Kassner, M.E., King, W.E., McNelley, T.R., McQueen, H.J., Rollett, A.D., 1997. Current issues in recrystallization: a review. Mater. Sci. Eng. A 238, 219–274.
Drury, M.R., Pennock, G.M., 2007. Subgrain Rotation Recrystallization in Minerals. Mater. Sci. Forum 550, 95–104.
Dubosq, R., Lawley, C.J.M., Rogowitz, A., Schneider, D.A., Jackson, S., 2018. Pyrite deformation and connections to gold mobility: Insight from micro-structural analysis and trace element mapping. Lithos 310–311, 86–104.
Earth impact database. http://www.passc.net/EarthImpactDatabase/New%20website_05-2018/Index.html.
Engelhardt, W.V., Matthäi, S.K., Walzebuck, J., 1992. Araguainha impact crater, Brazil. I. The interior part of the uplift. Meteoritics 27, 442–457.
Erickson, T.M., Cavosie, A.J., Moser, D.E., Barker, I.R., Radovan, H.A., Wooden, J., 2013a. Identification and provenance determination of distally transported, Vredefort-derived shocked minerals in the Vaal River, South Africa using SEM and SHRIMP-RG techniques. Geochim. Cosmochim. Acta 107, 170–188.
Erickson, T.M., Cavosie, A.J., Moser, D.E., Barker, I.R., Radovan, H.A., 2013b. Correlating planar microstructures in shocked zircon from the Vredefort Dome at multiple scales: Crystallographic modeling, external and internal imaging, and EBSD structural analysis. Am. Mineral. 98, 53–65.
Erickson, T.M., Pearce, M.A., Taylor, R.J.M., Timms, N.E., Clark, C., Reddy, S.M., Buick, I.S., 2015. Deformed monazite yields high-temperature tectonic ages. Geology 43, 383–386.
Erickson, T.M., Cavosie, A.J., Pearce, M.A., Timms, N.E., Reddy, S.M., 2016. Empirical constraints on shock features in monazite using shocked zircon inclusions. Geology 44, 635–638.
Erickson, T.M., Timms, N.E., Kirkland, C.L., Tohver, E., Cavosie, A.J., Pearce, M.A., Reddy, S.M., 2017. Shocked monazite chronometry: integrating microstructural and in situ isotopic age data for determining precise impact ages. Contrib. to Mineral. Petrol. 172, 11.
Erickson, T.M., Kirkland, C.L., Timms, N.E., Cavosie, A.J., Davison, T.M., 2020. Precise radiometric age establishes Yarrabubba, Western Australia, as Earth's oldest recognised meteorite impact structure. Nat. Commun. 11, 300.
Fackelman, S.P., Morrow, J.R., Koeberl, C., McElvain, T.H., 2008. Shatter cone and microscopic shock-alteration evidence for a post-Paleoproterozoic terrestrial impact structure near Santa Fe, New Mexico, USA. Earth Planet. Sci. Lett. 270, 290–299.
Fletcher, I.R., Rasmussen, B., McNaughton, N.J., 2000. SHRIMP U-Pb geochronology of authigenic xenotime and its potential for dating sedimentary basins. Aust. J. Earth Sci. 47, 845–859.
Fletcher, I.R., McNaughton, N.J., Aleinikoff, J.A., Rasmussen, B., Kamo, S.L., 2004. Improved calibration procedures and new standards for U - Pb and Th - Pb dating of Phanerozoic xenotime by ion microprobe. Chem. Geol. 209, 295–314.
Flowers, R.M., Moser, D.E., Hart, R.J., 2003. Evolution of the Amphibolite-Granulite Facies Transition Exposed by the Vredefort Impact Structure, Kaapvaal Craton, South Africa. J. Geol. 111.
Fougerouse, D., Reddy, S.M., Saxey, D.W., Rickard, W.D.A., van Riessen, A., Micklethwaite, S., 2016. Nanoscale gold clusters in arsenopyrite controlled by growth rate not concentration: Evidence from atom probe microscopy. Am. Mineral. 101, 1916–1919.
Fougerouse, D., Reddy, S.M., Saxey, D.W., Erickson, T.M., Kirkland, C.L., Rickard, W.D.A., Seydoux-Guillaume, A.-M., Clark, C., Buick, I.S., 2018. Nanoscale distribution of Pb in monazite revealed by atom probe microscopy. Chem. Geol. 479, 251–258.
Fougerouse, D., Reddy, S.M., Kirkland, C.L., Saxey, D.W., Rickard, W.D., Hough, R.M., 2019. Time-resolved, defect-hosted, trace element mobility in deformed Witwatersrand pyrite. Geosci. Front. 10, 55–63.
Fougerouse, D., Cavosie, A.J., Erickson, T., Reddy, S.M., Cox, M.A., Saxey, D.W., Rickard, W.D.A., Wingate, M.T.D., 2021a. A new method for dating impact events – Thermal dependency on nanoscale Pb mobility in monazite shock twins. Geochim. Cosmochim. Acta 314, 381–396.
Fougerouse, D., Reddy, S.M., Seydoux-Guillaume, A.-M., Kirkland, C.L., Erickson, T.M., Saxey, D.W., Rickard, W.D.A., Jacob, D., Leroux, H., Clark, C., 2021b. Mechanical twinning of monazite expels radiogenic lead. Geology 49, 417–421.
Fougerouse, D., Saxey, D.W., Rickard, W.D.A., Reddy, S.M., Verberne, R., 2021c. Standardizing Spatial Reconstruction Parameters for the Atom Probe Analysis of Common Minerals. Microsc. Microanal. 1–10.
Gibson, R.L., Armstrong, R.A., Reimold, W.U., 1997. The age and thermal evolution of the Vredefort impact structure: A single-grain U-Pb zircon study. Geochim. Cosmochim. Acta 61, 1531–1540.
Gibson, R.L., Reimold, W.U., Stevens, G., 1998. Thermal-metamorphic signature of an impact event in the Vredefort dome, South Africa. Geology 26, 787–790.
Gibson, R.L., Reimold, W.U., 2005. Shock pressure distribution in the Vredefort impact structure, South Africa. In Large Meteorite Impacts III (eds. T. Kenkmann, F. Hörz, and A. Deutsch). Geological Society of America. 384, 329–349.
Grieve, R., Therriault, A., 2000. Vredefort, Sudbury, Chicxulub: Three of a Kind? Annu. Rev. Earth Planet. Sci. 28, 305–338.
Gumsley, A., Stamsnijder, J., Larsson, E., Söderlund, U., Naeraa, T., de Kock, M., Sałacińska, A., Gawęda, A., Humbert, F., Ernst, R., 2020. Neoarchean large igneous provinces on the Kaapvaal Craton in southern Africa re-define the formation of the Ventersdorp Supergroup and its temporal equivalents. GSA Bull. 132, 1829–1844.
Harrison, T.M., Catlos, E.J., Montel, J.-M., 2002. U-Th-Pb Dating of Phosphate Minerals. Rev. Mineral. Geochemistry 48, 524–558.
Hart, R.J., Nicolaysen, L.O., Gale, N.H., 1981. Radioelement concentrations in the deep profile through Precambrian basement of the Vredefort structure. J. Geophys. Res. Solid Earth 86, 10639–10652.
Hauser, N., Reimold, W.U., Cavosie, A.J., Crósta, A.P., Schwarz, W.H., Trieloff, M., Maia, D.S., de Souza, C., Pereira, L.A., Rodrigues, E.N., Brown, M., 2019. Linking shock textures revealed by BSE, CL, and EBSD with U-Pb data (LA-ICP-MS and SIMS) from zircon from the Araguainha impact structure, Brazil. *Meteorit. Planet. Sci.* 54, 2286–2311.
Hetherington, C.J., Jercinovic, M.J., Williams, M.L., Mahan, K., 2008. Understanding geologic processes with xenotime: Composition, chronology, and a protocol for electron probe microanalysis. Chem. Geol. 254, 133–147.
Hiraga, T., Anderson, I.M., Kohlstedt, D.L., 2003. Chemistry of grain boundaries in mantle rocks. Am. Mineral. 88, 1015–1019.
Hodych, J.P., Dunning, G.R., 1992. Did the Manicouagan impact trigger end-of-Triassic mass extinction? Geology 20, 51–54.
Hoskin, P.W.O., Black, L.P., 2000. Metamorphic zircon formation by solid-state recrystallization of protolith igneous zircon. J. Metamorph. Geol. 18, 423–439.
Jessell, M.W., 1987. Grain-boundary migration microstructures in a naturally deformed quartzite. J. Struct. Geol. 9, 1007–1014.
Joseph, C., Fougerouse, D., Saxey, D.W., Verberne, R., Reddy, S.M., Rickard, W.D.A., 2021. Xenotime at the Nanoscale: U-Pb Geochronology and Optimisation of Analyses by Atom Probe Tomography. Geostand. Geoanalytical Res. 45, 443–456.
Joseph, C., Fougerouse, D., Reddy, S.M., Olierook, H.K.H., Tacchetto, T., Kennedy, A., Saxey, D.W., Rickard, W.D.A., Denyszyn, S., Dodd, A., 2023. Radiogenic Pb in xenotime trapped in nanoscale inclusions of apatite during fluid alteration. Chem Geol., 121444
Jourdan, F., Renne, P.R., Reimold, W.U., 2009. An appraisal of the ages of terrestrial impact structures. Earth Planet. Sci. Lett. 286, 1–13.
Jourdan, F., Reimold, W.U., Deutsch, A., 2012. Dating terrestrial impact structures. Elements 8, 49–53.
Kamo, S.L., Reimold, W.U., Krogh, T.E., Colliston, W.P., 1996. A 2.023 Ga age for the Vredefort impact event and a first report of shock metamorphosed zircons in pseudotachylitic breccias and Granophyre. Earth Planet. Sci. Lett. 144, 369–387.
Kamo, S.L., Lana, C., Morgan, J.V., 2011. U-Pb ages of shocked zircon grains link distal K–Pg boundary sites in Spain and Italy with the Chicxulub impact. Earth Planet. Sci. Lett. 310, 401–408.
Kenkmann, T., 2021. The terrestrial impact crater record: A statistical analysis of morphologies, structures, ages, lithologies, and more. Meteorit. Planet. Sci. 56, 1024–1070.
Kenny, G.G., Morales, L.F., Whitehouse, M.J., Petrus, J.A., Kamber, B.S., 2017. The formation of large neoblasts in shocked zircon and their utility in dating impacts. Geology 45, 1003–1006.
Kenny, G.G., Harrigan, C.O., Schmitz, M.D., Crowley, J.L., Wall, C.J., Andreoli, M.A.G., Gibson, R.L., Maier, W.D., 2021. Timescales of impact melt sheet crystallization and the precise age of the Morokweng impact structure, South Africa. *Earth Planet. Sci. Lett.* 567, 117013.
Kirkland, C.L., Yakymchuk, C., Szilas, K., Evans, N., Hollis, J., McDonald, B., Gardiner, N. J., 2018. Apatite: a U-Pb thermochronometer or geochronometer? Lithos 318–319, 143–157.
Lana, C., Filho, C.R.S., Marangoni, Y.R., Yokoyama, E., Trindade, R.I.F., Tohver, E., Reimold, W.U., 2007. Insights into the morphology, geometry, and post-impact erosion of the Araguainha peak-ring structure, central Brazil. GSA Bull. 119, 1135–1150.
Lana, C., Filho, C.R.S., Marangoni, Y.R., Yokoyama, E., Trindade, R.I.F., Tohver, E., Reimold, W.U., 2008. Structural evolution of the 40 km wide Araguainha impact structure, central Brazil. Meteorit. Planet. Sci. 43, 701–716.
Langenhorst, F., Deutsch, A., 2012. Shock Metamorphism of Minerals. Elements 8, 31–36.
Li, Q.L., Li, X.H., Lan, Z.W., Guo, C.L., Yang, Y.N., Liu, Y., Tang, G.Q., 2013. Monazite and xenotime U-Th-Pb geochronology by ion microprobe: Dating highly fractionated granites at Xihuashan tungsten mine, SE China. *Contrib. to Mineral. Petrol.* 166, 65–80.
Love, G.R., 1964. Dislocation pipe diffusion. Acta Metall. 12, 731–737.

Ludwig, K., 2012. User's manual for Isoplot/Ex: a geochronological toolkit for Microsoft Excel. Berkeley Geochronol. *Cent. Spec. Publ.* 1a, 53.
Machado, R., Lana, C., Stevens, G., Filho, C.R.S., Reimold, W.U., McDonald, I., 2009. Generation, mobilization and crystallization of impact-induced alkali-rich melts in granitic target rocks: Evidence from the Araguainha impact structure, central Brazil. Geochim. Cosmochim. Acta 73, 7183–7201.
McGregor, M., McFarlane, C.R.M., Spray, J.G., 2018. In situ LA-ICP-MS apatite and zircon U-Pb geochronology of the Nicholson Lake impact structure, Canada: Shock and related thermal effects. Earth Planet. Sci. Lett. 504, 185–197.
McGregor, M., McFarlane, C.R.M., Spray, J.G., 2019. In situ multiphase U-Pb geochronology and shock analysis of apatite, titanite and zircon from the Lac La Moinerie impact structure, Canada. *Contrib. Mineral. Petrol.* 174, 62.
McGregor, M., Dence, M.R., McFarlane, C.R.M., Spray, J.G., 2020. U-Pb geochronology of apatite and zircon from the Brent impact structure, Canada: a Late Ordovician Sandbian-Katian boundary event associated with L-Chondrite parent body disruption. Contrib. Mineral. Petrol. 175, 63.
McGregor M., McFarlane C. R. M. and Spray J. G. (2021) U-Pb geochronology of apatite crystallized within a terrestrial impact melt sheet: Manicouagan as a geochronometer test site eds. W. U. Reimold and C. Koeberl. Large Meteor. Impacts Planet. Evol. VI 550, 0.
McNaughton, N.J., Rasmussen, B., Fletcher, I.R., 1999. SHRIMP uranium-lead dating of diagenetic xenotime in siliciclastic sedimentary rocks. Science 285, 78–80.
McNaughton, N.J., Rasmussen, B., 2018. Geochemical characterisation of xenotime formation environments using U-Th. Chem. Geol. 484, 109–119.
Montalvo, P.E., Cavosie, A.J., Kirkland, C.L., Evans, N.J., McDonald, B.J., Talavera, C., Erickson, T.M., Lugo-Centeno, C., 2019a. Detrital shocked zircon provides first radiometric age constraint (<1472 Ma) for the Santa Fe impact structure, New Mexico, USA. GSA Bull. 131, 845–863.
Montalvo, S.D., Reddy, S.M., Saxey, D.W., Rickard, W.D.A., Fougerouse, D., Quadir, Z., Johnson, T.E., 2019b. Nanoscale constraints on the shock-induced transformation of zircon to reidite. Chem. Geol. 507, 85–95.
Montalvo S. D. (2020) Development and application of atom probe tomography to complex zircon grains, 169.
Moser, D.E., 1997. Dating the shock wave and thermal imprint of the giant Vredefort impact, South Africa. Geology 25, 7–10.
Moser, D.E., Cupelli, C.L., Barker, I.R., Flowers, R.M., Bowman, J.R., Wooden, J., Hart, J. R., 2011. New zircon shock phenomena and their use for dating and reconstruction of large impact structures revealed by electron nanobeam (EBSD, CL, EDS) and isotopic U-Pb and (U-Th)/he analysis of the Vredefort dome. Can. J. Earth Sci. 48, 117–139.
Ni, Y., Hughes, J.M., Mariano, A.N., 1995. Crystal chemistry of the monazite and xenotime structures. Am. Mineral. 80, 21–26.
O'Neill, C., Marchi, S., Zhang, S., Bottke, W., 2017. Impact-driven subduction on the Hadean Earth. Nat. Geosci. 10, 793–797.
Osinski, G.R., Cockell, C.S., Pontefract, A., Sapers, H.M., 2020. The role of meteorite impacts in the origin of life. Astrobiology 20, 1121–1149.
Osinski, G.R., Grieve, R.A.F., Ferrière, L., Losiak, A., Pickersgill, A.E., Cavosie, A.J., Hibbard, S.M., Hill, P.J.A., Bermudez, J.J., Marion, C.L., Newman, J.D., Simpson, S. L., 2022. Impact Earth: A review of the terrestrial impact record. Earth-Science Rev. 232, 104112.
Pan, Y., Fleet, M.E., 2002. Compositions of the apatite-group minerals: substitution mechanisms and controlling factors. Rev. Mineral. Geochemistry 48, 13–49.
Papapavlou, K., Darling, J.R., Moser, D.E., Barker, I.R., White, L.F., Lightfoot, P.C., Storey, C.D., Dunlop, J., EIMF, 2018. U-Pb isotopic dating of titanite microstructures: potential implications for the chronology and identification of large impact structures. Contrib. Mineral. Petrol. 173, 82.
Passchier C. W. and Trouw R. A. J. (2005) Micro-tectonics., second ed. Springer Berlin, Heidelberg.
Peterman, E.M., Reddy, S.M., Saxey, D.W., Snoeyenbos, D.R., Rickard, W.D.A., Fougerouse, D., Kylander-Clark, A.R.C., 2016. Nanogeochronology of discordant zircon measured by atom probe microscopy of Pb-enriched dislocation loops. Sci. Adv. 2.
Peterman, E.M., Reddy, S.M., Saxey, D.W., Fougerouse, D., Snoeyenbos, D.R., Rickard, W.D.A., 2019. Nanoscale processes of trace element mobility in metamorphosed zircon. Contrib. to Mineral. Petrol. 174, 92.
Piazolo, S., Austrheim, H., Whitehouse, M., 2012. Brittle-ductile microfabrics in naturally deformed zircon: Deformation mechanisms and consequences for U-Pb dating. Am. Mineral. 97, 1544–1563.
Piazolo, S., La Fontaine, A., Trimby, P., Harley, S., Yang, L., Armstrong, R., Cairney, J.M., 2016. Deformation-induced trace element redistribution in zircon revealed using atom probe tomography. Nat. Commun. 7, 1–7.
Poirier J.-P. (1985) Creep of Crystals: High-Temperature Deformation Processes in Metals, Ceramics and Minerals., Cambridge University Press, Cambridge.
Rasmussen, B., 2005. Radiometric dating of sedimentary rocks: The application of diagenetic xenotime geochronology. Earth-Science Rev. 68, 197–243.
Read, A.S., Koning, D.J., Smith, G.A., Ralser, S., Rodgers, J.B., Bauer, P.A., 2000. geologic map of Santa Fe quadrangle, Santa Fe County, New Mexico New Mexico Bureau of Geology and mineral resources. Open-File GM 32 scale 124,000, 1 sheet.
Reddy, S.M., van Riessen, A., Saxey, D.W., Johnson, T.E., Rickard, W.D.A., Fougerouse, D., Fischer, S., Prosa, T.J., Rice, K.P., Reinhard, D.A., Chen, Y., Olson, D., 2016. Mechanisms of deformation-induced trace element migration in zircon resolved by atom probe and correlative microscopy. Geochim. Cosmochim. Acta 195, 158–170.
Rickard, W.D.A., Reddy, S.M., Saxey, D.W., Fougerouse, D., Timms, N.E., Daly, L., Peterman, E., Cavosie, A.J., Jourdan, F., 2020. Novel Applications of FIB-SEM-based ToF-SIMS in atom probe tomography workflows. Microsc. Microanal. 26, 750–757.
Schmieder, M., Kring, D.A., 2020. Earth's impact events through geologic time: A list of recommended ages for terrestrial impact structures and deposits. Astrobiology 20, 91–141.
Schmieder, M., Tohver, E., Jourdan, F., Denyszyn, S.W., Haines, P.W., 2015. Zircons from the Acraman impact melt rock (South Australia): Shock metamorphism, U-Pb and 40 Ar/ 39 Ar systematics, and implications for the isotopic dating of impact events. Geochim. Cosmochim. Acta 161, 71–100.
Schmieder, M., Shaulis, B.J., Lapen, T.J., Buchner, E., Kring, D.A., 2019. In situ U-Pb analysis of shocked zircon from the Charlevoix impact structure, Québec, Canada. *Meteorit. Planet. Sci.* 54, 1808–1827.
Schneiderhan, E., Zimmermann, U., Gutzmer, J., Mezger, K., Armstrong, R., 2011. Sedimentary Provenance of the Neoarchean Ventersdorp Supergroup, Southern Africa: shedding light on the evolution of the Kaapvaal Craton during the Neoarchean. J. Geol. 119, 575–596.
Schulte, P., Alegret, L., Arenillas, I., Arz, J.A., Barton, P.J., Bown, P.R., Bralower, T.J., Christeson, G.L., Claeys, P., Cockell, C.S., Collins, G.S., Deutsch, A., Goldin, T.J., Goto, K., Grajales-Nishimura, J.M., Grieve, R.A.F., Gulick, S.P.S., Johnson, K.R., Kiessling, W., Koeberl, C., Kring, D.A., MacLeod, K.G., Matsui, T., Melosh, J., Montanari, A., Morgan, J.V., Neal, C.R., Nichols, D.J., Norris, R.D., Pierazzo, E., Ravizza, G., Rebolledo-Vieyra, M., Reimold, W.U., Robin, E., Salge, T., Speijer, R.P., Sweet, A.R., Urrutia-Fucugauchi, J., Vajda, V., Whalen, M.T., Willumsen, P.S., 2010. The chicxulub asteroid impact and mass extinction at the cretaceous-paleogene boundary. Science 327, 1214–1218.
Seydoux-Guillaume, A.-M., Fougerouse, D., Laurent, A.T., Gardés, E., Reddy, S.M., Saxey, D.W., 2019. Nanoscale resetting of the Th/Pb system in an isotopically-closed monazite grain: A combined atom probe and transmission electron microscopy study. Geosci. Front. 10, 65–76.
Shannon, R.D., 1976. Revised effective ionic radii and systematic studies of interatomic distances in halides and chalcogenides. Acta Crystallogr. Sect. A 32, 751–767.
Spear, F.S., Pyle, J.M., 2002. Apatite, monazite, and xenotime in metamorphic rocks (in Phosphates; geochemical, geobiological, and materials importance) Reviews in Mineralogy and Geochemistry. Rev. Mineral. Geochemistry 48, 293–335.
Stacey, J.S., Kramers, J.D., 1975. Approximation of terrestrial lead isotope evolution by a two-stage model. Earth Planet. Sci. Lett. 26, 207–221.
Stöffler, D., Hamann, C., Metzler, K., 2018. Shock metamorphism of planetary silicate rocks and sediments: Proposal for an updated classification system. Meteorit. Planet. Sci. 53, 5–49.
Suzuki, K., 1987. Grain-boundary enrichment of incompatible elements in some mantle peridotites. Chem. Geol. 63, 319–334.
Tacchetto, T., Reddy, S.M., Saxey, D.W., Fougerouse, D., Rickard, W.D.A., Clark, C., 2021. Disorientation control on trace element segregation in fluid-affected low-angle boundaries in olivine. Contrib. to Mineral. Petrol. 176, 1–16.
Tacchetto, T., Reddy, S.M., Fougerouse, D., Clark, C., Saxey, D.W., Rickard, W.D.A., 2022. Crystal plasticity enhances trace element mobility in garnet. Geology 50, 1387–1392.
Timms, N.E., Erickson, T.M., Pearce, M.A., Cavosie, A.J., Schmieder, M., Tohver, E., Reddy, S.M., Zanetti, M.R., Nemchin, A.A., Wittmann, A., 2017. A pressure-temperature phase diagram for zircon at extreme conditions. Earth-Science Rev. 165, 185–202.
Timms, N.E., Kirkland, C.L., Cavosie, A.J., Rae, A.S.P., Rickard, W.D.A., Evans, N.J., Erickson, T.M., Wittmann, A., Ferrière, L., Collins, G.S., Gulick, S.P.S., 2020. Shocked titanite records Chicxulub hydrothermal alteration and impact age. Geochim. Cosmochim. Acta 281, 12–30.
Tohver, E., Lana, C., Cawood, P.A., Fletcher, I.R., Jourdan, F., Sherlock, S., Rasmussen, B., Trindade, R.I.F., Yokoyama, E., Souza, F.C.R., Marangoni, Y., 2012. Geochronological constraints on the age of a Permo-Triassic impact event: U-Pb and 40Ar/39Ar results for the 40km Araguainha structure of central Brazil. Geochim. Cosmochim. Acta 86, 214–227.
Valley, J.W., Cavosie, A.J., Ushikubo, T., Reinhard, D.A., Lawrence, D.F., Larson, D.J., Clifton, P.H., Kelly, T.F., Wilde, S.A., Moser, D.E., Spicuzza, M.J., 2014. Hadean age for a post-magma-ocean zircon confirmed by atom-probe tomography. Nat. Geosci. 7, 219–223.
Vallini, D.A., Rasmussen, B., Krapež, B., Fletcher, I.R., McNaughton, N.J., 2005. Microtextures, geochemistry and geochronology of authigenic xenotime: Constraining the cementation history of a Palaeoproterozoic metasedimentary sequence. Sedimentology 52, 101–122.
Van Emden, B., Thornber, M.R., Graham, J., Lincoln, F.J., 1997. The incorporation of actinides in monazite and xenotime from placer deposits in Western Australia. Can. Mineral. 35, 95–104.
Verberne, R., Reddy, S.M., Saxey, D.W., Fougerouse, D., Rickard, W.D.A., Plavsa, D., Agangi, A., Kylander-Clark, A.R.C., 2020. The geochemical and geochronological implications of nanoscale trace-element clusters in rutile. Geology 48, 1–5.
Verberne, R., Reddy, S.M., Saxey, D.W., Fougerouse, D., Rickard, W.D.A., Quadir, Z., Evans, N.J., Clark, C., 2022. Dislocations in minerals: Fast-diffusion pathways or trace-element traps? Earth Planet. Sci. Lett. 584, 117517.
Vermeesch, P., 2018. IsoplotR: A free and open toolbox for geochronology. Geosci. Front. 9, 1479–1493.
Watanabe, T., 1985. Structural effects on grain boundary segregation, hardening and fracture. Le J. Phys. Colloq. 46. C4–555-C4-566.
White, L.F., Darling, J.R., Moser, D.E., Reinhard, D.A., Prosa, T.J., Bullen, D., Olson, D., Larson, D.J., Lawrence, D., Martin, I., 2017. Atomic-scale age resolution of planetary events. Nat. Commun. 8, 1–6.
Williams, C.A., Haley, D., Marquis, E.A., Smith, G.D.W., Moody, M.P., 2013. Defining clusters in APT reconstructions of ODS steels. Ultramicroscopy 132, 271–278.
Williams, M.L., Jercinovic, M.J., Harlov, D.E., Budzyń, B., Hetherington, C.J., 2011. Resetting monazite ages during fluid-related alteration. Chem. Geol. 283, 218–225.